Experimental and numerical investigation of circular concrete-filled steel tubular columns subjected to post-earthquake fires

Guo-Qiang Wei [a], Wen-Da Wang [a,b,*], Kan Zhou [c], Wen-Jing Mao [a,b]

[a]*School of Civil Engineering, Lanzhou University of Technology, Lanzhou 730050, China*

[b]*Shanghai Key Laboratory of Engineering Structure Safety, SRIBS, Shanghai 200032, China*

[c]*School of Built Environment, Engineering and Computing, Leeds Beckett University, City Campus, Leeds, LS1 3HE, UK*

Abstract: Fires induced by earthquakes are high-probability events that can accelerate the collapse of buildings. This research investigates the fire resistance of eight circular concrete-filled steel tubular (CFST) columns under four earthquake damage levels through experimental methods. The earthquake damage and fire tests were conducted continuously without unloading the axial loads. The impact of earthquake damage levels and axial load ratios on fire resistance were studied. The failure mode, temperature evolution, fire performance, and deformation of the columns under post-earthquake fire (PEF) were analyzed and discussed. In addition, the validated numerical method was used to simulate the fire resistance of the columns that suffered seismic damage. The results show that the maximum axial expansion of the columns gradually decreases with increasing seismic damage. When the axial load ratio is 0.284, a slight decrease in fire resistance occurs at drift ratios exceeding 2.67%, and plastic hinges form at the mid-height of the column at failure. When the drift ratio reaches 4.48%, premature lateral displacement induces a more pronounced second-order effect, accelerating column instability and leading to a significant decrease in fire resistance. At an axial load ratio of 0.431, although the lateral stiffness of the column decreases more severely, fire resistance exhibits only a slight reduction at a drift ratio of 4.42%.

Keywords: Seismic damage; Fire resistance; Post-earthquake fire (PEF); Cyclic loading; Finite element analysis (FEA); Concrete-filled steel tubular column (CFST)

*Corresponding author at: School of Civil Engineering, Lanzhou University of Technology, Lanzhou, China
E-mail: wangwd@lut.edu.cn (W.-D. Wang)

1. Introduction

Fire is the most common secondary hazard induced by earthquakes. Historical seismic records indicate that PEF disasters are high-probability events that cause enormous destruction. In the 1906 San Francisco earthquake and 1923 Tokyo earthquake, the damage caused by PEFs was three times than that caused by the earthquakes themselves. There are more than 100 fire accidents were reported in the 1994 Northridge earthquake and 1995 Kobe earthquake [1-3]. The reduction in structural strength and stiffness, residual deformation, a flake of fire coating, failure of firefighting systems, and leakage of flammable material caused by the earthquake reduced the fire performance of buildings and increased collapse probability.

To clarify the performance of structures subjected to PEF, researchers have carried out numerous studies on the fire resistance of reinforced concrete frames (Sharma *et al*. [4]; Kamath *et al*. [5]; Shah *et al*. [6]; Behnam *et al*. [7]; Vitorino *et al*. [8]) and steel frames (Jelinek *et al*. [9]; Memari *et al*. [10]; Suwondo *et al*. [11]) suffered seismic damage. It was found that the levels of damage corresponding to life safety (LS) had an insignificant effect on fire resistance [4-6, 9-11]. Concrete spalling, residual deformation, and stiffness degradation after earthquakes reduce the bearing capacity of the structure under fire [7, 8]. It was reported that uneven fire distribution after an earthquake increased the risk of structural collapse [10, 11]. Song *et al*. [12, 13] studied the fire resistance of square steel tube columns-steel beam joints after earthquake damage experimentally and numerically. It was found that steel fracture and residual stress caused by cyclic loading greatly reduced the PEF performance. Pucinotti *et al*. [14] analysed the fire performance of composite connections after seismic damage based on seismic tests. The analysis showed that energy dissipation occurred mainly at the beam ends, and the effects of earthquake damage on fire performance were marginal.

Concrete-filled steel tubular (CFST) has been widely applied in various structures such as buildings, bridges, and industrial constructions due to its numerous excellent properties [15]. Its fire performance has been a concern owing to the exposed steel tube. Many experimental studies (Lie and Chabot [16]; Han *et al.* [17]; Yang *et al.* [18]; Xiong and Liew [19]; Xiong *et al.* [20]) have focused on the mechanical

properties of undamaged CFST columns at high temperatures, and fire resistance calculation (Yu *et al.* [21]; Wang and Young [22]; Li and Hu [23]; Moradi *et al.* [24]) and design methods (Ukanwa *et al.* [25]; Albero *et al.* [26]) have been proposed. Wang *et al.*[27] and Medall *et al*. [28, 29] also conducted experimental research and numerical analysis on the fire resistance of steel-reinforced concrete-filled steel tubular (SRCFST) columns. Farhangi *et al*. [30] employed artificial intelligence (AI) techniques to predict the residual strength of fiber reinforced concrete (FRC) after exposure to elevated temperatures, deriving meaningful and valuable conclusions. Daneshvar *et al.* [31] conducted experimental and numerical studies on the impact performance of reinforced concrete slabs exposed to ISO-834 standard fire conditions. Qaidi *et al*. [32, 33] studied the effect of temperature on the mechanical properties of mine tailings-based geopolymers composites (MT-GPC) and crumb rubber concrete (CRC). From the above, it can be seen that for a long time, numerous scholars have extensively conducted experimental and numerical studies on undamaged CFST and SRCFST columns, leading to the development of well-established and mature design methods. However, research on fire resistance after earthquake damage is limited. Imani *et al*. [34, 35] investigated the fire performance of concrete-filled double-skin steel tubular columns after earthquake damage. They showed that seismic damage had a negligible impact on the fire performance when the columns were fixed at both ends, and the inner tube reinforcement significantly improved the PEF performance [36]. Wang *et al*. [37] carried out an experimental investigation on the PEF performance of square CFST columns, and a parametric analysis was conducted using the FEA method. A fire resistance calculation formula after seismic damage was proposed. Talebi *et al*. [38] numerically researched the performance of circular CFST columns subjected to PEF, showing that the damage location was the major factor influencing fire resistance.

Although limited research has been conducted on the PEF performance of columns, experimental studies specifically focusing on circular CFST columns under PEF conditions have not yet been reported. It is important to highlight that in existing PEF experimental studies [34, 37], the specimens were typically removed after completing the seismic damage tests and then reinstalled to conduct fire tests. This process could alter the seismic damage state and potentially affect the experimental results. In this

study, the cyclic loading and fire tests were conducted continuously without unloading the axial loads. This approach minimizes the effects of specimen removal and re-installation on the seismic damage state, and closely aligns with real post-earthquake fire scenarios.

This study first conducted a test study on the fire resistance of eight circular CFST columns after seismic damage. The axial load ratio (n) and seismic damage level were used as experimental parameters. The heating behavior, deformation, and failure modes were analysed. The reasons for the failure of the circular CFST columns under PEF were clarified. In addition, a numerical calculation method for PEFs is proposed and validated based on experimental results. Using the calibrated numerical models, the steel tube stress, core concrete strain, and axial force distribution were analyzed and discussed. The experimental and numerical research method in this research offer valuable insights in the design and reinforcement of CFST structures.

2. Experimental programme

The experiment was divided into two parts: a cyclic loading test (simulating earthquake damage) and an ISO-834 standard fire test (simulating PEF).

2.1 Design of specimens

Eight circular CFST specimens with the same geometric dimensions were designed based on the Chinese code GB50936-2014 [39]. The specimen length was 2900 mm, and two endplates measuring 240 mm × 240 mm × 20 mm were welded at both ends as shown in Fig. 1. The specimen was installed according to group 1 (C219-N3, C219-M3, C219-N5, C219-S5) and group 2 (C219-S3, C219-H3, C219-M5, C219-H5) to measure the cross-section temperature distributed at four heights (Sections A, B, C, D). Table 1 lists the geometric dimensions and loading information. The specimen labels are as follows: C219 means the diameter is 219 mm; N, S, M, and H refer to the seismic damage levels of no damage, slight damage, moderate damage, and high damage, respectively; 3 and 5 represent the axial load ratios of 0.3 and 0.5, respectively (with a deviation in the test). n is the axial load ratio ($n=N_0/N_u$, where N_0 is the axial load applied to the specimen, and N_u is the axial bearing capacity of an undamaged specimen at ambient temperature and calculated based on the code [39]). The axial loads are the same

for the seismic damage experiment and the fire experiment. Δ_y is the yield displacement estimated using the FEA method [15]. Δ_u is the maximum loading horizontal displacement, θ is the corresponding drift ratio ($\theta=\Delta_u/H$, where H is half the distance between the rotation centres of the two pin-supports). K represents the secant stiffness of the final loading cycle. t_e represents the measured fire resistance.

2.2 Material properties

A tensile experiment was conducted at ambient temperature on steel coupons cut from circular tubes and the results are shown in Table 2. Three groups of 150-mm concrete cubes were cured under the same temperature and humidity conditions as the specimens. The measured average concrete cube strength (f_{cu}) at 28 days and on the test day (240 days) was 28.6 MPa and 31.3 MPa, respectively.

2.3 Cyclic loading tests

Considering that column damage in an actual frame under seismic action primarily occurs near the beam-column joint, the mid-height of the column is used as the joint location for horizontal loading. The top and bottom of the columns are treated as inflection points of the frame and are allowed to rotate. Fig. 2 shows the schematic of the cyclic loading test, where the bottom and top boundary conditions of the specimens were hinged. The specimen was inserted into the two pin-supports and clamped with bolts to ensure that its geometric center was aligned with the rotation center of the pin-support. A load cell was installed between the specimen and the jack. Horizontal action was exerted on the mid-height of the column by the actuator. The horizontal displacement at the mid-height was recorded using transducers DT1 and DT2. The distribution of strain gauges is illustrated in Fig. 3, and steel tube strains were measured during cyclic loading. The designed axial force (N_0) was exerted on the specimen and kept it constant. Cyclic loads were applied in the displacement control pattern according to the loading protocol suggested by the Chinese standard JGJ/T101-2015 [40], as illustrated in Fig. 4(a). In the pre-yielding stage, displacement loading was performed at $0.25\Delta_y$, $0.5\Delta_y$, and $0.7\Delta_y$. During the post-yielding phase, the loading displacement increased in multiples of Δ_y. The damage levels of the specimens were determined according to FEMA 356 [41]. The observed damage of the CFST columns during the cyclic loading tests [15, 34, 37] should also be considered. FEMA 356 defines three seismic performance levels: Immediate Occupancy (IO), Life Safety (LS), and Collapse Prevention (CP), corresponding to drift ratios of 0.7%, 2.5%, and 5% for steel frames, and 1%, 2%, and 4% for reinforced

concrete frames, respectively. Considering that the mechanical properties of CFST frames are more similar to steel frames, the drift ratios of 1%, 2.5%, and 4.5% correspond to slight, moderate, and high damage, respectively. The drift ratios measured during the tests (noting that actual loading exhibited some deviations) are shown in Table 1. The degree of earthquake damage is represented by the displacement amplitude, which can be divided into four damage levels:

- No damage: Not subjected to cyclic loading tests (Specimens C219-N3 and C219-N5).
- Slight damage: At $1.0\Delta_y$(θ=0.88%-0.92%) level of cyclic loading, strain measurements indicated that the steel tubes had yielded and undergone plastic deformation. The loading was stopped at point A (Fig. 4) for specimens C219-S3 and C219-S5.
- Moderate damage: At $3.0\Delta_y$(θ=2.63%-2.67%) level, visible local buckling appeared on surfaces No. 1 and No. 2 (Fig. 3) of the steel tube. Specimens C219-M3 and C219-M5 stopped loading at point B (Fig. 4).
- High damage: At the $5.0\Delta_y$(θ=4.42%-4.48%) level, the local buckling of surfaces No. 1 and No. 2 became more severe, with signs of developing into annular buckling. The loading was stopped at point C (Fig. 4) for specimens C219-H3 and C219-H5.

2.4 Fire tests

When the displacement returns to zero during cyclic loading (points A, B, C in Fig. 4), the specimen still has a large lateral force. To eliminate this lateral force (residual drift), as shown in Fig. 4(b), when the displacement returns to zero at point N1, the specimen is further loaded to a displacement value (calculated based on the stiffness of the hysteresis curve from the previous loading cycle) to reach point N2. Then, the specimen is pulled back to point N3, where the displacement is zero, and the residual force becomes negligible. Subsequently, the connecting beam was removed (Fig. 2), and the actuator was shortened to allow space for the furnace installation. A detachable electric furnace was used to conduct the fire test. The setup diagram is shown in Fig. 5, the furnace cavity had dimensions of 700 mm in length, 700 mm in width, and 2000 mm in height, with both the upper and lower openings of the furnace blocked with ceramic fibre boards. The furnace is equipped with eight independent heating

plates, each with a thermocouple to monitor the furnace temperature distribution, as shown in Fig. 5(b). The boundary conditions and axial load were kept consistent with those in the cyclic loading test.

The column axial deformation was recorded using displacement sensors DT1, DT2, DT3, and DT4 installed at the corners of the sliding stub, as shown in Fig. 5(a). The average value from these sensors was taken as the final axial displacement. Two displacement transducers DWT1 and DWT2 connected to the mid-height using a high-temperature alloy wire were used to measure the horizontal displacement. The two displacement values were averaged to minimize the deviation caused by the elongation of the alloy wire and radial expansion of the steel tube at high temperatures. The furnace heating followed the ISO-834 standard curve [42]. Nine thermocouples were arranged to measure temperature evolution over time, as shown in Fig. 1(c). Temperature and displacement were recorded at intervals of 10 seconds and 1 second, respectively. Failure was defined as an axial shortening exceeding $0.01L$ (29 mm) or an axial shortening rate exceeding $0.003L$ per minute (8.7 mm/min) [42], at which point the test was terminated.

3. Test results and discussion

3.1 Damage after cyclic loading

Fig. 6 shows the local buckling of the steel tube after cyclic loading. No visible local buckling was observed in the steel tube for specimens C219-S3 and C219-S5 with a drift ratio of $1.0\Delta_y$, although strain measurements indicated that plastic deformation had occurred in a portion of the steel tube cross-sections. When the loading displacement increased to $3.0\Delta_y$ (specimens C219-M3 and C219-M5), local buckling occurred on surfaces No.1 and 2 of the steel tube. The local buckling in specimen C219-M5 was more severe than in C219-M3. When the loading reached $5.0\Delta_y$ (specimens C219-H3 and C219-H5), the degree of local buckling on surfaces No.1 and 2 increased sharply, and the buckled region extended to surfaces No.3 and 4. Steel tubes develop severe damage for specimens with loading displacement exceeding $3.0\Delta_y$, which may reduce the fire performance.

The hysteretic curves are shown in Fig. 7. It is apparent that the hysteresis curves for the columns at the two axial load levels are similar. It is noteworthy that the horizontal bearing capacity of specimens C219-H3 and C219-H5 decreased to 93.7% and 88.6% of their ultimate load-bearing capacity,

respectively. The secant stiffness [40] of the final loading cycle are shown in Table 1. For the specimens with n=0.284 and n=0.431, the secant stiffness values for the first loading cycle were 7.43 kN/mm and 7.56 kN/mm, respectively. It is evident that the stiffness of the specimen with n=0.284 decreased from 7.43 kN/mm to 1.23 kN/mm, while the specimen with n=0.431 exhibited a reduction from 7.56 kN/mm to 1.09 kN/mm. This further indicates that strength and stiffness degradation is accelerated, and the damage is more severe for larger axial compression ratio conditions.

3.2 Failure modes after PEF

The column failure modes subjected to PEF are illustrated in Fig. 8. The steel tube exhibited a grey-black color with areas of dark red. All specimens failed owing to global buckling. For specimens with n=0.283, the overall deformation of the slightly damaged specimen C219-S3 is similar to that of the undamaged specimen C219-N3. Specimen C219-M3 developed a plastic hinge in the seismic damaged region as the damage degree increased, which became more pronounced in specimen C219-H3. At n=0.431, specimens C219-N5, C219-S5, and C219-M5 exhibited similar overall deformation, while specimen C219-H5 developed a plastic hinge at the seismic damage location. The plastic hinge in the specimen with n=0.283 is more obvious than that in the specimen with n=0.431 under the same degree of seismic damage. The possible reasons are as follows: (1) the specimen with n=0.283 was exposed to a longer fire duration (23 min), resulting in higher steel tube temperatures (650 ℃) at failure, which led to greater deformation on the tensile side. (2) Under seismic damage conditions, second-order effects are more pronounced in specimens with n=0.283 at elevated temperatures. Additionally, when the cyclic loading displacement exceeds $3.0\Delta_y$ (with a drift ratio of 2.6%), local buckling of the steel tubes is confined to the area near the clamp, with no local buckling observed elsewhere. The local buckling induced by seismic damage progresses into more severe outward bulging at elevated temperatures (Fig. 8c, d, g, and h). This indicates that the moderate seismic damage, corresponding to a drift rate of 2.6%, significantly affects the specimen failure mode under fire.

As illustrated in Fig. 9, the core concrete of the specimen with n=0.284 was exposed after the steel tube was cut away. It is evident that the transverse tensile cracks of specimens C219-N3 and C219-S3

were evenly distributed on the tensile side. Notably, no concrete crushing was observed near the clamp areas. With increasing seismic damage, the spacing of the transverse cracks in specimen C219-M3 decreased and became concentrated in the seismic damaged area (near the clamp), accompanied by concrete crushing on the compression side within that region. For specimen C219-H3, wider transverse cracks were evident on the tensile side, and more severe crushing on the compression side can be observed for core concrete. The spalling of concrete on the tensile side indicated significant crushing in the specimen under cyclic loading conditions before the elevated temperature. It can be concluded that the preexisting cracks induced by earthquake damage on the tensile side continued to propagate, while the crushing on the compression side further deteriorated, for CFST columns subjected to PEF.

3.3 Temperature distributions

The furnace temperatures and the temperatures of typical measuring points are shown in Figs. 10 and 11, respectively. The furnace temperatures recorded by the thermocouples on each heating plate are essentially the same, and the temperature curves of different sections (A, B, C, and D) are also nearly identical, indicating that the temperature distribution within the furnace cavity is uniform. A comparison of the average furnace temperature of all specimens and the ISO-834 standard curve is illustrated in Fig. 10(b). The measured furnace temperature generally matches well with the standard curve, with a slight delay occurring before the 7th min. Notably, the variation in furnace temperature among the specimens was minimal, ensuring consistent temperature conditions for comparing the fire resistance of specimens with varying degrees of damage. The heating curves of typical measuring points are depicted in Fig. 11, showing a rapid increase in the steel tube temperature. A turning point in the temperature curve is observed at the 7th min of heating, consistent with the trend observed in the furnace heating curves (Fig. 10).

The temperature at the concrete measurement point rose slowly, and the temperature development remained constant or fluctuated around 100 °C at approximately the 6th min for the partial concrete measurement point. This may be related to the evaporation of water contained in the concrete at high temperatures. Two conditions may have occurred during the test: (1) due to installation or cyclic loading,

the thermocouple may not have been in close contact with the concrete, leading to the measurement of void temperatures (possibly steam) in the concrete. (2) As moisture unevenly distributed in the concrete evaporates at elevated temperatures, heat migrates inside the concrete, dissipating some of the heat. It should be noted that although there was a slight temperature deviation at the same coordinate measuring point for specimens with varying degrees of damage, the discrepancy had no obvious regularity. Therefore, seismic damage is regarded to have a negligible effect on the heating of the CFST column.

3.4 Deformation and fire resistance

The time histories of axial and lateral displacements are shown in Fig. 12. The initial axial compression displacement before heating has been eliminated, and the curve can be divided into four stages.

(1) Thermal expansion: Due to the steel tube thermal expansion, the axial deformation curve initiates an upward trend and reaches its maximum value. The duration of this stage varies between 7-14 min depending on the axial load levels. The axial displacement-time curve of specimens with n=0.284 exhibited a notable inflection point around the 7th minute, consistent with the temperature trend of the steel tubes (refer to Fig. 11). It is evident that seismic damage has minimal impact during this phase.

(2) Stable deformation: During this stage, the axial expansion deformation plateaus and reaches an equilibrium state as the steel tube bearing capacity degrades gradually. Specimens C219-H3 and C219-H5 experienced shorter durations in this phase owing to severe seismic damage.

(3) Gradual decrease: The axial displacement starts to decrease as the steel tube bearing capacity continues to deteriorate. Specimens with n=0.284 exhibited a rapid initial decrease in axial and lateral displacements, followed by a slower decline until a sudden drop at the onset of the fourth phase.

(4) Decrease sharply: The axial and lateral displacement experienced a sudden, sharp increase, leading to specimen failure and the termination of the test.

Fig. 13 illustrates a comparison of the deformation at elevated temperatures for specimens subjected to different levels of seismic damage. When n=0.284, the deformation curve of the specimen

exhibited rapid development, followed by a gradual slowdown. This may be attributed to the increasing temperature, which caused the steel tube to fail to bear the axial force, causing rapid shortening until the endplate contacted the core concrete again. Notably, the deformation curve of specimen C219-H3 showed a significant increase at the 13th minute. This premature lateral displacement led to a more pronounced second-order effect, accelerating the specimen failure. There are three possible reasons for this. Firstly, the steel tube was compressed from time T2 to T3 (Figs. 13 and 14), which aggravated the existing mid-height local buckling. Secondly, the steel tube bears the main tension of the CFST section. As displayed in Fig. 14, the original bulge on the tension side was first flattened by tension (from time T2 to T3) at elevated temperatures, which reduced the steel tube's tensile capacity. Thirdly, the damaged concrete on the compression side was prematurely crushed at high temperatures. These results indicate that seismic damage led to a decrease in the lateral bearing capacity of the specimen. The greater the degree of earthquake damage, the more significant the reduction in lateral stiffness. Similarly, when n=0.431, the axial displacement curves of specimens C219-M5 and C219-H5 showed a sudden decrease at the 7th and 12th min, respectively. This may be attributed to the larger axial load resulting in smaller axial expansion. Noteworthy, the fire resistance of specimen C219-H5 decreased by only 0.5 min compared to C219-N5. This could be because all the specimens were not sprayed with fireproof coatings. In particular, the fire resistance of the specimen C219-N5 (undamaged) is relatively low (14.2 min), leading to a less pronounced decrease in fire resistance. Additionally, the fire exposure time for the specimen with n=0.431 was relatively short (14 min), and the temperature of the steel tube at the time of failure was between 470℃ and 500℃. It is possible that the deformation of the steel tube at this temperature did not significantly impact the fire resistance of the specimen. Compared to the specimen with n=0.284, the sudden development in axial and lateral displacements occurred earlier and with a smaller magnitude. The comparison of these displacement evolutions indicates that the axial load and seismic damage levels have an important influence on the deformation during high temperatures.

Figs. 13 and 15(a) show a comparison of axial expansion evolution and maximum axial expansion of specimens with different seismic damage degrees, respectively. The maximum axial expansion of

no-damage specimens decreases from 11.17 mm to 5.14 mm, as n increases from 0.284 to 0.431. As seismic damage increased, the maximum axial expansion of the specimens with n=0.284 and n=0.431 decreased from 11.17 mm to 8.78 mm and from 5.14 mm to 3.61 mm, respectively. It should be noted that the maximum axial expansion for specimens C219-S3 and C219-S5 decreased by 0.65 mm compared to the undamaged specimens. This indicates that the steel tube local buckling caused by seismic damage reduces the axial stiffness of the CFST column at high temperatures. Although steel tube local buckling was not found in the specimens with drift rates of 0.88%-0.92%, there was still a slight decrease in axial expansion.

A comparison of the fire resistance for columns with four levels of earthquake damage is presented in Table 1 and Fig. 15(b), and the moment when the specimen became unstable and reached the fire resistance (t_e) is marked with a red cross in Fig 12. It was found that an increase in the axial load ratio from 0.284 to 0.431 resulted in a reduction of fire resistance for the undamaged specimens, from 22.3 min to 14.2 min, respectively. As the level of earthquake damage increased, the damaged specimens showed varying degrees of reduction in fire resistance. Notably, the column at an axial compression ratio of 0.284 experienced a more significant decrease. There was no significant deviation in the fire resistance values for specimens C219-S3 and C219-S5 compared to the undamaged specimens. When θ=2.63-2.67%, the fire resistance of specimen C219-M3 decreased to 20.7 min, while specimen C219-M5 showed a slight increase. This may be due to the specimen fabrication and loading deviation. When θ=4.42-4.48%, the fire resistance of specimen C219-H3 decreased to 16.8 min, and specimen C219-H5 decreased to 13.4 min. It was observed that the earthquake damage corresponding to an axial drift ratio of 0.87% had no effect on fire resistance, but when θ>2.6%, the fire resistance of the specimen with n=0.284 decreased more significantly.

Fig.16 illustrates the influence of axial load ratio and seismic damage on the reduction rate of fire resistance. At a drift ratio of 0.9%, the fire resistance remained unchanged for both axial load ratios. When the drift ratio increased to 2.5%, the fire resistance of the specimen with n=0.284 decreased to 94%, while that of the specimen with n=0.431 remained unchanged. At a drift ratio of 4.5%, fire

resistance dropped to 74.6% and 94.6%, respectively. Notably, the specimen with n=0.431 experienced more severe seismic damage and a greater reduction in lateral stiffness (Section 3.1). This deviation may be attributed to the relatively short fire exposure time in this group, possibly limiting the impact of seismic damage (Section 3.4).

4. Numerical investigation

Although the experiment can reflect the actual state of specimens subjected to a PEF, the boundary conditions, section size, and fire modes of the specimens were limited. Previous experimental conclusions have been obtained with specific boundary conditions and fire modes [12, 13, 34, 37]. However, the effects of PEFs on structures are more intricate owing to the randomness of earthquakes and fires. The FEA method can be used as a supplement to research the behavior of structures subjected to PEFs under different boundary conditions and fire modes, and to further analyze their working mechanism.

4.1 Development of FEA models

An FEA method was developed based on the ABAQUS software to simulate the behavior of circular CFST columns under PEF. The analysis flowchart is shown in Fig. 17. The method was first established to simulate the cyclic loading tests, and the deformation results from this analysis were imported into the temperature field model to study the effect of steel tube local bucking on the temperature distribution. Thereafter, the stress and deformation states after the cyclic load analysis were taken as the initial state of the thermal-stress model. The same meshing was used for the above three models to obtain an accurate temperature reading and damage-state import, as shown in Fig. 18.

4.1.1 Cyclic loading FEA model

The core concrete and steel tube were modelled by selecting C3D8R and S4R elements, respectively, which have been widely used in seismic and fire performance analysis of CFST specimens [15, 18, 35, 37, 38]. As shown in Fig. 18, a reference point was established at the bottom pin-support rotation center. The "coupling" constraint was used between the reference point and the steel tube, and between the reference point and concrete. The axial load was applied to the loading plate. "Surface-to-

surface contact" was employed for the interactions between the loading plate and concrete, while the interaction between the loading plate and the steel tube was modeled using "shell-solid coupling." The thickness of the loading plate corresponded to the distance from the specimen end to the rotation center of the upper pin-support. The interaction between steel tube and core concrete was defined by surface-to-surface contact, in which the normal and tangential interactions were simulated by "Hard contact" and "Coulomb friction" (friction coefficient=0.6 [15]), respectively. The bilinear kinematic hardening model considering the Bauschinger effect was used to simulate the steel properties under cyclic loading. It was assumed that the hardening stiffness was $0.01E_s$, and that the steel strength no longer increased after reaching the tensile strength (f_u) [15, 43]. The concrete damage plastic model (CDP) in ABAQUS was applied for concrete; its compressive performance used the stress–strain relationship proposed by Han [15], considering the steel tube restraint. The tensile performance of concrete was expressed by Hillerborg *et al*. [44]. The damage variables in the CDP model were calculated using the method proposed by Li *et al*. [43]. To clarify the material characteristics and element types used in FEA models at different analysis stages, a summary is presented in Table 3.

4.1.2 Temperature-field FEA model

The DS4 and DC3D8 elements were selected for the uncoupled heat transfer analysis of the steel tube and concrete, respectively. The actual furnace heating curve (Fig. 10) was used in the temperature-field FEA model, and the impact of deformation due to seismic damage on the temperature-field analysis was considered. The temperature was transferred to the steel tube surface by means of thermal radiation and convection. The film coefficient and radiation emissivity were 50 W/(m^2·°C) and 0.5, respectively. The thermal parameters presented by Lie [45] were used for the steel tube and concrete. The concrete moisture was assumed to be 5% to consider the effect of water vapor caused by the temperature effect [46]. Different degrees of voids occurred between the steel tubes and concrete after cyclic loading. Contact thermal resistance will occur due to an air-gap across the steel-concrete interface. Ding and Wang [47] studied the relationship between the thermal resistance coefficient and fire resistance for undamaged CFST columns. A thermal resistance coefficient of 0.01 (m^2·°C)/W was

proposed, which has been validated against various test data [48-50]. However, for CFST columns that have experienced seismic damage, the gap between the outer steel tube and the concrete may change, potentially enlarging locally, and is related to the levels of seismic damage. There are no relevant reports or test data to investigate this complex effect. Thus, thermal contact resistance with a value of 0.01 $(m^2 \cdot °C)/W$ was introduced in the analysis of heat transfer between steel tube and concrete.

4.1.3 Thermal-stress FEA model

A thermal-stress FEA model was used to analyze the fire performance of circular CFST specimens subjected to PEF. The boundary conditions, elements, and meshing were the same as those in the cyclic loading model. The thermal-stress analysis considers the geometrical deformation, plastic strain, and stress state resulting from seismic damage. However, due to the complex interaction between earthquake damage and elevated temperature, as well as the lack of experimental data on their relationship, the material property degradation caused by seismic damage has not been incorporated into the thermal-stress model. The CDP model was used as the concrete constitutive model at high temperatures, and the calculation method for compression performance proposed by Han [15] was used. The stress-fracture energy model proposed by Han *et al.* [46] was applied to describe the tensile properties. The stress-strain relationship of the steel tube at high temperatures suggested by Lie [45] was employed. In addition, the thermal expansion was calculated based on the formula given by Lie [45]. The Poisson's ratio of concrete was 0.2 at ambient temperature and calculated at a high temperature according to Gernay *et al.* [51]. To account for the effects of initial bending and installation eccentricity, an initial eccentricity of $L/1000$ was considered in the FEA, while L denotes the column length.

4.2 Validation of FEA model

Based on the failure modes, fire performance, and heating characteristics obtained from the tests, the FEA method was calibrated to improve the accuracy of the numerical simulations. Fig. 6 shows the damage modes after cyclic loading obtained using the FEA model. It is apparent that the location and degree of steel tube local buckling are consistent with the experimental observations. As shown in Fig. 7, the calculated hysteretic curves agreed well with the test results regarding horizontal bearing capacity,

stiffness, and energy dissipation capacity, although there were deviations in the strength degradation. This deviation may be due to the axial load in the numerical simulation being a constant value, while there were some fluctuations of axial load applied by the jack in the test.

A comparison of the failure modes observed in the tests and those predicted by the numerical simulations is presented in Fig. 19, taking specimens C219-S3 and C219-H3 as an example. The failure modes in the numerical simulations closely resembled those observed experimentally. Specimen C219-S3 exhibited overall bending deformation, and specimen C219-H3 exhibited obvious plastic hinges in the mid-height. Furthermore, earthquake damage led to a high equivalent plastic strain at the mid-hight position in the steel tube. Fig. 19 also shows the maximum principal plastic strain of the concrete, in which the development direction of the concrete tensile crack is illustrated by the arrow direction (i.e. the direction perpendicular to the maximum principal plastic strain) [15]. It is observed that the distribution of tensile cracks is consistent in the simulation and the test. It is speculated that the developed FEA calculation method in this research could accurately transfer the deformation and stress state induced by cyclic loading to the thermal-stress model.

The comparison between the simulated temperature and the measured is displayed in Fig. 11. Overall, the temperature values calculated for the steel tube agree well with the measured results, although it is lower than the measured temperature. In addition, the simulated temperature obtained by concrete was lower than that in the experimental data due to moisture in the concrete. The heat migration and removal in concrete caused by moisture evaporation was not achieved in FEA, although the impact of moisture was indirectly accounted for by adjusting the specific heat capacity of the concrete. Additionally, the position deviation of the thermocouple embedding also affected the temperature at the measuring point.

Fig. 12 and Fig. 15(b) show a comparison of the deformation and fire resistance results from the FEA and experimental measurements, respectively. Furthermore, the fire performance tests of CFDST [34] and square CFST [37] specimens after earthquake damage were also simulated, as shown in Fig. 20. The tested axial expansion deformation is larger than the FEA results in Fig.12. This deviation may

be due to seismic damage causing local buckling of the steel tube, which increased the gap between the steel tube and the concrete. The resulting thermal resistance could not be accurately accounted for in the FEA. Additionally, deviations in the film coefficient, radiation emissivity, and thermal conductivity in the FEA from their actual values may have contributed to the thermal expansion discrepancy. Although some differences exist, the simulated deformation evolution and fire resistance are in good agreement with the experimental data, and the trend of fire resistance reduction is also generally consistent (Fig. 16). These discrepancies may be attributed to inevitable initial imperfections and boundary conditions. The initial eccentricity of axial loading was assumed to be $L/1000$ (2.9 mm) in the FEA. However, the actual initial loading eccentricity may vary owing to the installation deviation of the specimen. Additionally, the boundary conditions in the FEA assumed ideal hinge and free-rotation conditions at both ends of the column, whereas, they may have been constrained by friction as the axial force increased during the test. It is important to note that these deviations are common and difficult to eliminate in tests owing to the complexity of cyclic loads and fire tests. In general, the numerical method employed in this study provides a reasonable prediction of the fire resistance and deformation of damaged CFST columns under high temperatures, effectively reflecting the reduction in fire resistance caused by earthquake damage.

4.3 Axial load distribution

Fig. 21 presents the axial force distribution of the steel tube and concrete for specimens with different seismic damage degrees. The axial load distribution ratio is defined as the proportion of the total axial load (N_0) carried by either the steel tube or the core concrete. It was found that the evolutions of the axial load distribution trends for all specimens exhibited similar patterns. Before heating, when n=0.283, the steel tube axial load distribution ratios were 0.505, 0.498, 0.443, and 0.368 for C219-N3, C219-S3, C219-M3, and C219-H3, respectively. Correspondingly, for specimens with n=0.431, the axial load distribution ratios of the steel tubes were 0.465, 0.463, 0.368, and 0.275, respectively. The major axial load can be borne by core concrete at ambient temperature due to the larger sectional area. After heating began, the axial force is gradually transferred from the concrete to the steel tube, in line

with the increasing expansion deformation of the steel tube. The axial load distribution ratio of the steel tube for C219-N3 and C219-H3 reached 1.0 at the 5th and 8th min, respectively. This indicates that the steel tube bears the entire axial force because of the separation of the top endplate and concrete, which corroborates the speculation made in Section 3.4. The maximum axial load distribution ratio supported by the steel tube for C219-N5 was 0.899, while the maximum ratios for C219-M5 and C219-H5 were 0.843 and 0.706, respectively. This observation could be attributed to the decreased steel tube axial bearing capacity both before heating and during the fire in specimens with seismic damage exceeding a drift ratio of 2.5%. In addition, the steel tube and concrete of specimens C219-M3 and C219-H3 began to share axial loading and deformation again at 13 and 15.5 minutes, respectively. By this time, the steel tube had already experienced significant axial compressive deformation (Fig. 12), and the initial local buckling at mid-height may have been further exacerbated. In contrast, specimens C219-M5 and C219-H5 shared loading and deformation throughout. This explains why the more pronounced plastic hinge deformation in the specimen with n=0.284 compared to that with n=0.431. It further indicated that the cumulative deformation and stress induced by initial earthquake damage significantly influence the fire resistance of circular CFST columns.

4.4 Stress and strain distribution

Fig. 22 illustrates the stress distribution of the steel tube and the strain distribution of the concrete for specimens with n=0.284, as obtained from the FEA. It can be seen that the stress values of the steel tube for columns C219-N3 and C219-S3 are higher in the mid-height area and evenly distributed. The core concrete tensile strain of specimen C219-S3 is concentrated in the previously damaged areas, indicating that the damage corresponding to a 0.87% drift ratio may have already caused cracking in the concrete, and the cracks further widened under subsequent high temperatures. For specimens C219-M3 and C219-H3, the magnitude of the steel tube stress further increased and was concentrated at the local buckling position caused by the earthquake damage. Correspondingly, the compressive strain in the core concrete further increased and became more focused in the previously damaged areas. This

indicates that when the drift ratio is 2.5%, compressive damage had already occurred in the concrete, further aggravated by the subsequent fire.

The FEA results reveal that when the drift ratio exceeds 2.5%, the steel tube stress and the concrete strain are concentrated in the mid-height area of the column. The steel tube axial bearing capacity shows a substantial reduction, and the axial and lateral stiffness of the column also reduces accordingly. This results in the column showing a plastic hinge at the previously damaged area when it fails at high temperature, rather than exhibiting overall bending deformation.

5. Conclusions

In this study, cyclic loading experiments and fire experiments were conducted to evaluate the PEF performance of eight circular CFST columns. An FEA method of CFST columns that suffered PEF was proposed and verified. The study investigated the effects of axial load levels and earthquake damage on the fire resistance of the columns. The following conclusions were drawn:

(1) The influence of earthquake damage on the fire performance of circular CFST columns diminishes as the axial load ratio increases. For n=0.284, the fire resistance decreased from 21.7 minutes (undamaged) to 20.6 minutes at a 2.67% drift ratio (θ), and further decreased to 16.2 minutes at θ=4.48%. For n =0.431, no reduction in fire resistance was observed at θ=2.63%, while the fire resistance decreased from 14.2 minutes (undamaged) to 13.7 minutes at θ=4.42%.

(2) The failure mode of circular CFST columns under PEF conditions is influenced by the extent of seismic damage and axial load ratio (n). For n=0.284, the damaged column with a θ=0.92% exhibited overall bending deformation similar to the undamaged column. When θ>2.67%, a plastic hinge at mid-height caused column failure at θ=4.48%. For n=0.431, all the columns exhibited overall bending deformation.

(3) Seismic damage led to a decrease in lateral stiffness, with the stiffness of the specimen with n=0.284 decreasing from 7.43 kN/mm to 1.23 kN/mm, while the specimen with n=0.431 showed a reduction from 7.56 kN/mm to 1.09 kN/mm. The specimen with n=0.284 at θ=4.48% experienced a

significant lateral displacement at high temperatures prematurely, and the second-order effect was more pronounced, accelerating the failure of the column.

(4) The numerical method was proposed and calibrated based on test results. Stress, strain, and axial load distributions were analyzed and compared for circular CFST columns with varying degrees of earthquake damage. Cyclic loading with a drift ratio exceeding 2.5% resulted in a notable diminish in the steel tube axial bearing capacity. Additionally, the stress in the steel tube and the strain in the concrete were significantly increased and concentrated in the damaged areas.

Acknowledgements

The authors would like to thank of the National Natural Science Foundation of China (Grant No. 52408179) partly, the Open project of Shanghai Key Laboratory of Engineering Structure Safety (Grant No. 2023-KF05), the Foundation for Innovation Groups of Basic Research in Gansu Province (Grant No. 24JRRA169), and the Youth Science and Technology Fund of Gansu Province (Grant No. 23JRRA807) for the financial support for this research.

References

[1] Scawthorn C, O'Rourke TD, Blackburn FT. The 1906 San Francisco earthquake and fire: enduring lessons for fire protection and water supply. *Earthquake Spectra* 2006; 22(S2): S135-S158.

[2] Nishino T, Tsuburaya SI, Himoto K, Tanaka T. A study on the estimation of the evacuation behaviors of Tokyo city residents in the Kanto earthquake fire. *Proceedings of 9th Symposium*. International Association for Fire Safety Science 2008; 453-464.

[3] Scawthorn C, Chen WF. Earthquake engineering handbook. CRC press: BocaRaton, FL; 2002.

[4] Sharma UK, Kumar V, Kamath P, Singh B, Bhargava P, Singh Y, Usmani A, Torero J, Gillie M, Pankaj P. Testing of full-scale RC frame under simulated fire following earthquake. *Journal of Structural Fire Engineering* 2014; 5(3): 215-228.

[5] Kamath P, Sharma UK, Kumar V, Bhargava P, Usmani A, Singh B, Singh Y, Torero J, Gillie M, Pankaj P. Full-scale fire test on an earthquake-damaged reinforced concrete frame. *Fire Safety Journal* 2015; 73: 1-19.

[6] Shah AH, Sharma UK, Pradeep B. Outcomes of a major research on full scale testing of RC frames in post earthquake fire. *Construction and Building Materials* 2017; 155: 1224-1241.

[7] Behnam B, Pang JL, Ronagh HR. Plastic hinge relocation in reinforced concrete frames as a method of improving post-earthquake fire resistance. *Structures* 2015; 2: 21-31.

[8] Vitorino H, Rodrigues H, Couto C. Evaluation of post-earthquake fire capacity of a reinforced concrete one bay plane frame under ISO fire exposure. *Structures* 2020; 23: 602-611.

[9] Jelinek T, Zania V, Giuliani L. Post-earthquake fire resistance of steel buildings. *Journal of Constructional Steel Research* 2017; 138: 774-782.

[10] Memari M, Mahmoud H, Ellingwood B. Post-earthquake fire performance of moment resisting frames with reduced beam section connections. *Journal of Constructional Steel Research* 2014; 103: 215-229.

[11] Suwondo R, Cunningham L, Gillie M, Bailey C. Progressive collapse analysis of composite steel frames subject to fire following earthquake. *Fire Safety Journal* 2019; 103: 49-58.

[12] Song QY, Heidarpour A, Zhao XL, Han LH. Post-earthquake fire behavior of welded steel I-beam to hollow column connections: an experimental investigation. *Thin-Walled Structures* 2016; 98: 143-153.

[13] Song QY, Heidarpourb A, Zhao XL, Han LH. Post-earthquake fire performance of flange-welded/web-bolted steel I-beam to hollow column tubular connections. *Thin-Walled Structures* 2017; 116: 113-123.

[14] Pucinotti R, Bursi OS, Demonceau JF. Post-earthquake fire and seismic performance of welded steel-concrete composite beam-to-column joints. *Journal of Constructional Steel Research* 2011; 67(9): 1358-1375.

[15] Han LH. Concrete filled steel tubular structures-theory and practice, 3rd edition. Science Press: Beijing, China; 2016: 30-66.

[16] Lie TT, Chabot M. Experimental studies on the fire resistance of hollow steel columns filled with plain concrete. NRC-CNRC internal report, No. 611, Ottawa(Canada); 1992.

[17] Han LH, Zhao XL, Yang YF, Feng JB. Experimental study and calculation of fire resistance of concrete-filled hollow steel columns. *Journal of Structural Engineering* 2003; 129: 346-356.

[18] Yang H, Liu FQ, Zhang SM, Lv XT. Experimental investigation of concrete-filled square hollow section columns subjected to non-uniform exposure. *Engineering Structures* 2013; 48: 292-312.

[19] Xiong MX, Liew JYR. Buckling behavior of circular steel tubes infilled with C170/185 ultra-high strength concrete under fire. *Engineering Structures* 2020; 212: 110523.

[20] Xiong Y, Lin KR, Wu D, Ling YH, Tesfamariam S. The role of a novel coating of SFRCR-ECC in enhancing the fire performance of CFST columns: Development, characteristic and ISO-834 standard fire test. *Engineering Structures* 2023; 294: 116629.

[21] Yu M, Zha XX, Ye JQ, Wang BL. A unified method for calculating fire resistance of solid and hollow concrete-filled steel tube columns based on average temperature. *Engineering Structures* 2014; 71: 12-22.

[22] Wang K, Young B. Fire resistance of concrete-filled high strength steel tubular columns. *Thin-Walled Structures* 2013; 71: 46-56.

[23] Li W, Hu J. Analytical modelling and critical temperature of circular CFST column exposed to standard fire. *Thin-Walled Structures* 2024; 200: 111900.

[24] Moradi MJ, Daneshvar K, Ghazi-nader D, Hajiloo H. The prediction of fire performance of concrete-filled steel tubes (CFST) using artificial neural network. *Thin-Walled Structures* 2021; 161: 107499.

[25] Ukanwa KU, Clifton GC, Lim JBP, Hicks SJ, Sharma U, Abu A. Simple design procedure for concrete filled steel tubular columns in fire. *Engineering Structures* 2018; 155: 144-156.

[26] Albero V, Espinós A, Romero ML, Wang YC, Renaud C, Schaumann P, Nigro E. Interaction diagram based method for fire resistance design of eccentrically loaded concrete-filled steel tubular columns. *Thin-Walled Structures* 2018; 130: 641-651.

[27] Wang WD, Mao WJ, Zhou K. Experimental investigation on residual capacity of steel-reinforced concrete-filled thin-walled steel tubular columns subjected to combined loading and temperature. *Thin-Walled Structures*, 2024, 197: 111557.

[28] Medall D, Ibáñez C, Espinós A, Romero ML. Experimental and numerical study of high-strength materials on slender steel-reinforced CFST columns in fire. *Thin-Walled Structures* 2025; 209: 112904.

[29] Medall D, EspinósA, Albero V, Romero ML. Simplified proposal for the temperature field of steel-reinforced CFST columns exposed to fire. *Engineering Structures* 2022; 273: 115083.

[30] Farhangi V, Moradi MJ, Daneshvar K, Hajiloo H. Application of artificial intelligence in predicting the residual mechanical properties of fiber reinforced concrete (FRC) after high temperatures. *Construction and Building Materials* 2024; 411: 134609.

[31] Daneshvar K, Moradi MJ, Khaleghi M, Rezaei M, Farhangi V, Hajiloo H. Effects of impact loads on heated-and-cooled reinforced concrete slabs. *Journal of Building Engineering* 2022; 61: 105328.

[32] Qaidi SMA, Tayeh BA, Zeyad AM, Azevedo ARG, Ahmed HU, Emad W. Recycling of mine tailings for the geopolymers production: A systematic review. *Case Studies in Construction Materials* 2022; 16, e00933.

[33] Qaidi SMA, Dinkha YZ, Haido JH, Ali MH, Tayeh BA. Engineering properties of sustainable green concrete incorporating eco-friendly aggregate of crumb rubber: A review. *Journal of Cleaner Production* 2021; 324: 129251.

[34] Imani R, Mosqueda G, Bruneau M. Experimental study on post-earthquake fire resistance of ductile concrete-filled double-skin tube columns. *Journal of Structural Engineering* 2015; 141(8): 04014192.

[35] Imani R, Mosqueda G, Bruneau M. Finite element simulation of concrete-filled double-skin tube columns subjected to post-earthquake fires. *Journal of Structural Engineering* 2015; 141(12): 04015055.

[36] Mohammadbagheri S, Shekastehband B. Fire resistance of stiffened CFDST columns after earthquake-induced damages. *Thin-Walled Structures* 2020; 154: 106865.

[37] Wang YH, Tang Q, Su MN, Tan JK, Wang WY, Lan YS, Luo W, Zhou Y. Post-earthquake fire performance of square concrete-filled steel tube columns. *Thin-Walled Structures* 2020; 154: 106873.

[38] Talebi E, Korzen M, Hothan S. The performance of concrete filled steel tube columns under post-earthquake fires. *Journal of Constructional Steel Research* 2018; 150: 115-128.

[39] GB50936-2014, Technical code for concrete filled steel tubular structures. China Architecture & Building Press: Beijing, China; 2014.

[40] JGJ/T101-2015. Specification for seismic test of buildings. China Architecture & Building Press: Beijing, China; 2015.

[41] FEMA356, Pre-standard and commentary for the seismic rehabilitation of buildings. Federal Emergency Management Agency, Washington DC; 2000.

[42] ISO 834-1, Fire-resistance tests-elements of building construction-part 1: general requirements. International Standards Organization, Switzerland; 1999.

[43] Li W, Han LH. Seismic performance of CFST column to steel beam joints with RC slab: Analysis. *Journal of Constructional Steel Research* 2011; 67: 127-139.

[44] Hillerborg A, Modeer M, Petersson PE. Analysis of crack formation and crack growth in concrete by means of fracture mechanics and finite elements. *Cement and Concrete Research* 1976; 6(6): 773-782.

[45] Lie TT. Fire resistance of circular steel columns filled with bar-reinforced concrete. *Journal of Structural Engineering* 1994; 120(5): 1489-1509.

[46] Han LH, Song TY, Zhou K. Fire Safety Design Theory of Steel-Concrete Composite Structures, 2rd edition. Science Press: Beijing, China; 2017.

[47] Ding J, Wang YC. Realistic modelling of thermal and structural behaviour of unprotected concrete filled tubular columns in fire. *Journal of Constructional Steel Research* 2008; 64(10): 1086-1102.

[48] Kordina K, Klingsch W. Fire resistance of composite columns of concrete filled hollow sections. Research report. CIDECT 15 C1/C2 - 83/27. Germany. 1983.

[49] Lie TT, Caron SE. Fire resistance of circular hollow steel columns filled with siliceous aggregate concrete. Test results, internal report no. 570. Ottawa (Canada): Institute for Research in Construction, National Research Council of Canada; 1988.

[50] Lie TT, Caron SE. Fire resistance of circular hollow steel columns filled with carbonate aggregate concrete. Test results, internal report no. 573. Ottawa (Canada): Institute for Research in Construction, National Research Council of Canada; 1988.

[51] Gernay T, Millard A, Franssen JM. A multiaxial constitutive model for concrete in the fire situation: theoretical formulation. *International Journal of Solids and Structures* 2013; 50(22-23): 3659-3673.

Tables

Table 1. Specimen details and test results

No.	Specimen label	$D\times t\times L$ (mm)	n	N_0 (kN)	Seismic damage level	Δ_u (mm)	θ (%)	K (kN/mm)	t_e (min)
1	C219-N3	219×3.95×2900	0.284	398	None	0	0	—	21.7
2	C219-S3	219×3.95×2900	0.284	398	Slight	14.1($1.0\Delta_y$)	0.92	5.51	22.2
3	C219-M3	219×3.95×2900	0.284	398	Moderate	40.8($3.0\Delta_y$)	2.67	2.28	20.6
4	C219-H3	219×3.95×2900	0.284	398	High	68.5($5.0\Delta_y$)	4.48	1.23	16.2
5	C219-N5	219×3.95×2900	0.431	593	None	0	0	—	14.2
6	C219-S5	219×3.95×2900	0.431	593	Slight	13.5($1.0\Delta_y$)	0.88	5.74	14.5
7	C219-M5	219×3.95×2900	0.431	593	Moderate	40.2($3.0\Delta_y$)	2.63	2.14	14.7
8	C219-H5	219×3.95×2900	0.431	593	High	67.7($5.0\Delta_y$)	4.42	1.09	13.7

Table 2. Mechanical properties of steel at ambient temperature

Yield strength f_y (MPa)	Ultimate strength f_u (MPa)	Young's modulus E_s (MPa)	Poisson's ration μ_s	Elongation δ (%)
297.5	395.06	2.12×10^5	0.303	26.81

Table 3 Summary of material constitutive and element types for different models

		Cyclic loading model	Temperature-field model	Thermal-stress model
Material models	Steel tube	Li *et al*. [43]	Lie (1994) [45]	Lie (1994) [45]
	Concrete	Han [15] (compression) Hillerborg *et al.* [44] (tensile) Li *et al*. [43] (damage)	Lie (1994) [45]	Han [15] (compression) Han *et al.* (2017) [46] (Tensile)
Elements	Steel tube	S4R	DS4	S4R
	Concrete	C3D8R	DC3D8	C3D8R

Figures

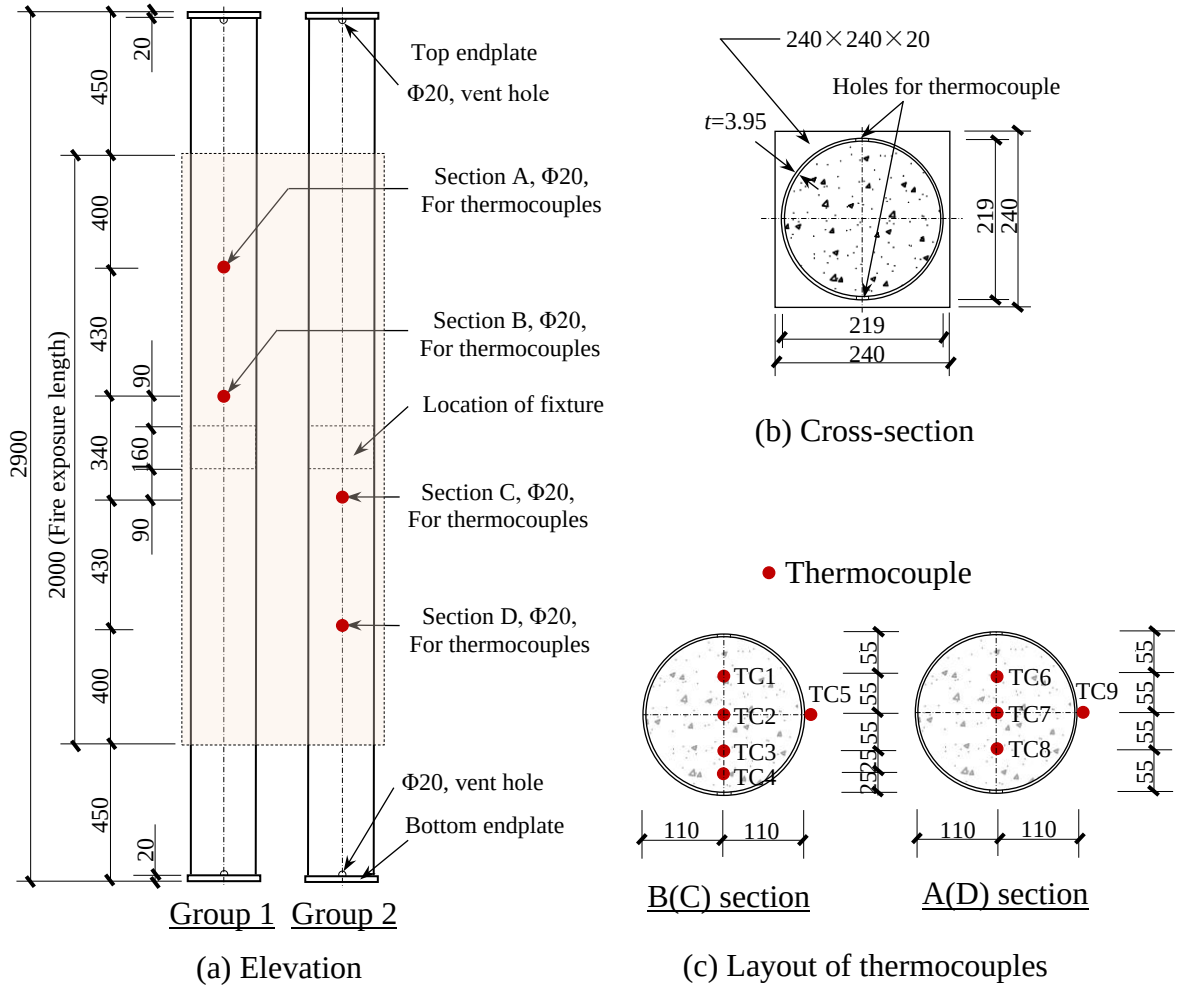

Fig. 1. Specimen details and layout of thermocouples (unit: mm)

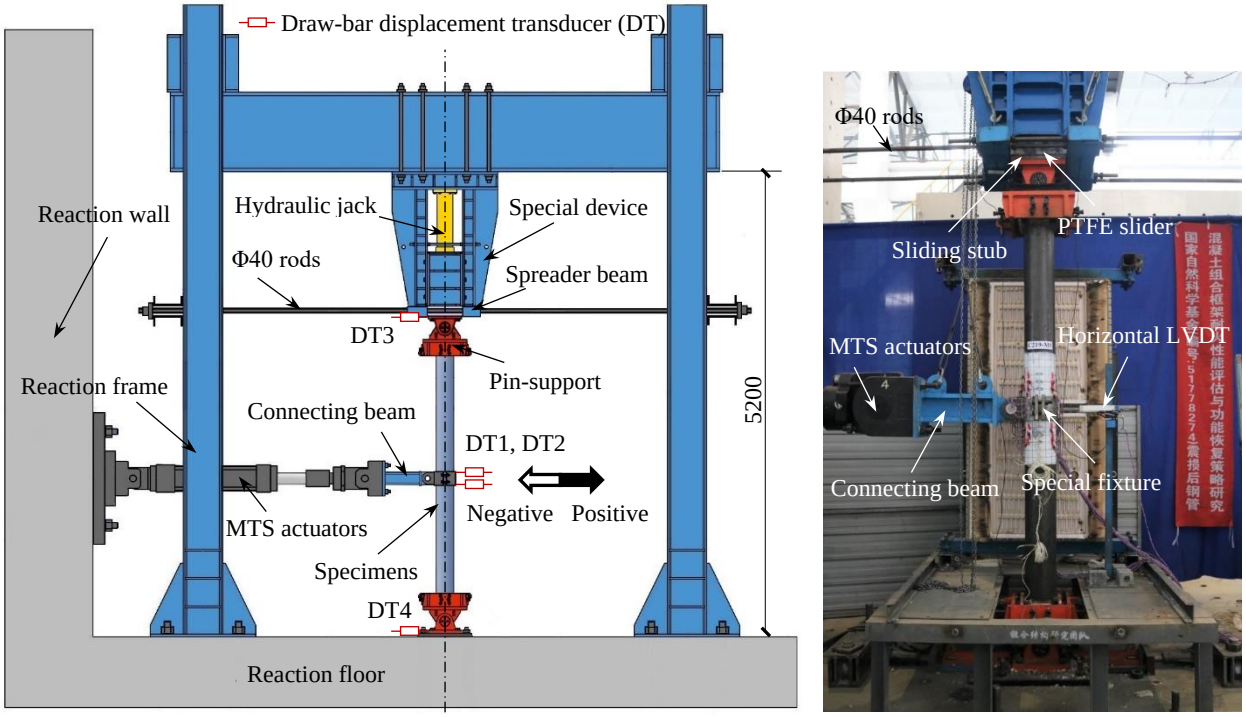

(a)Schematic (b) Photograph of test setup

Fig. 2. Test setup for cyclic loading (unit: mm)

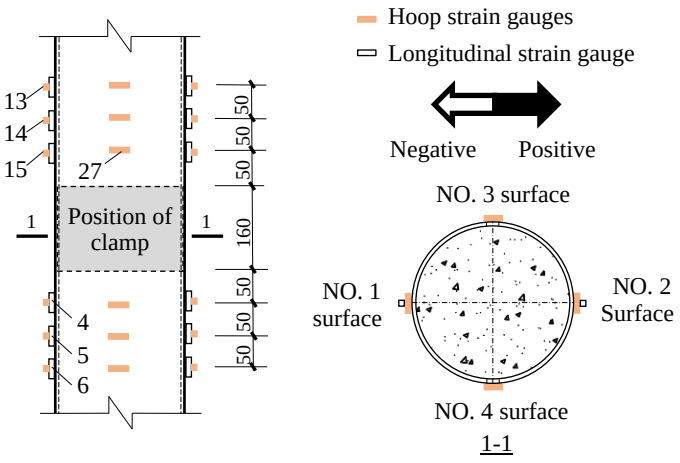

Fig. 3. Arrangement of strain gauges (unit: mm)

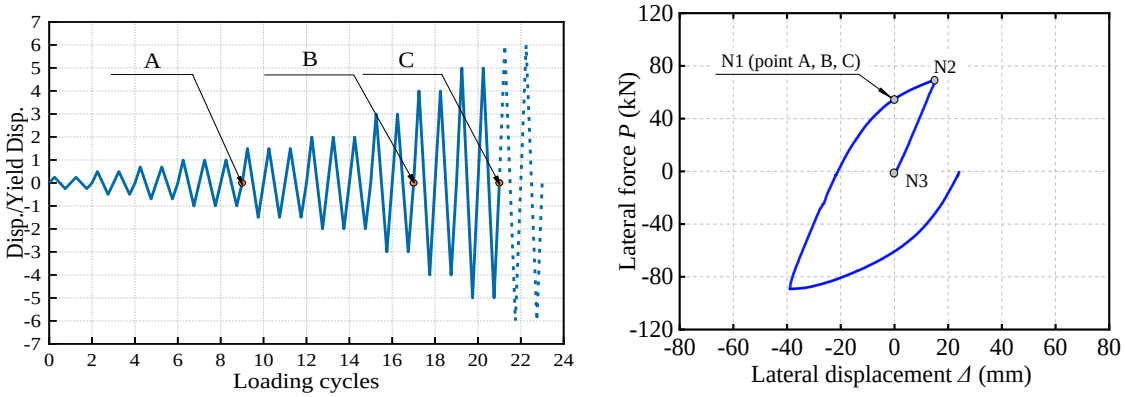

(a) Loading protocol (b) Schematic diagram of stop loading

Fig. 4. Loading protocol

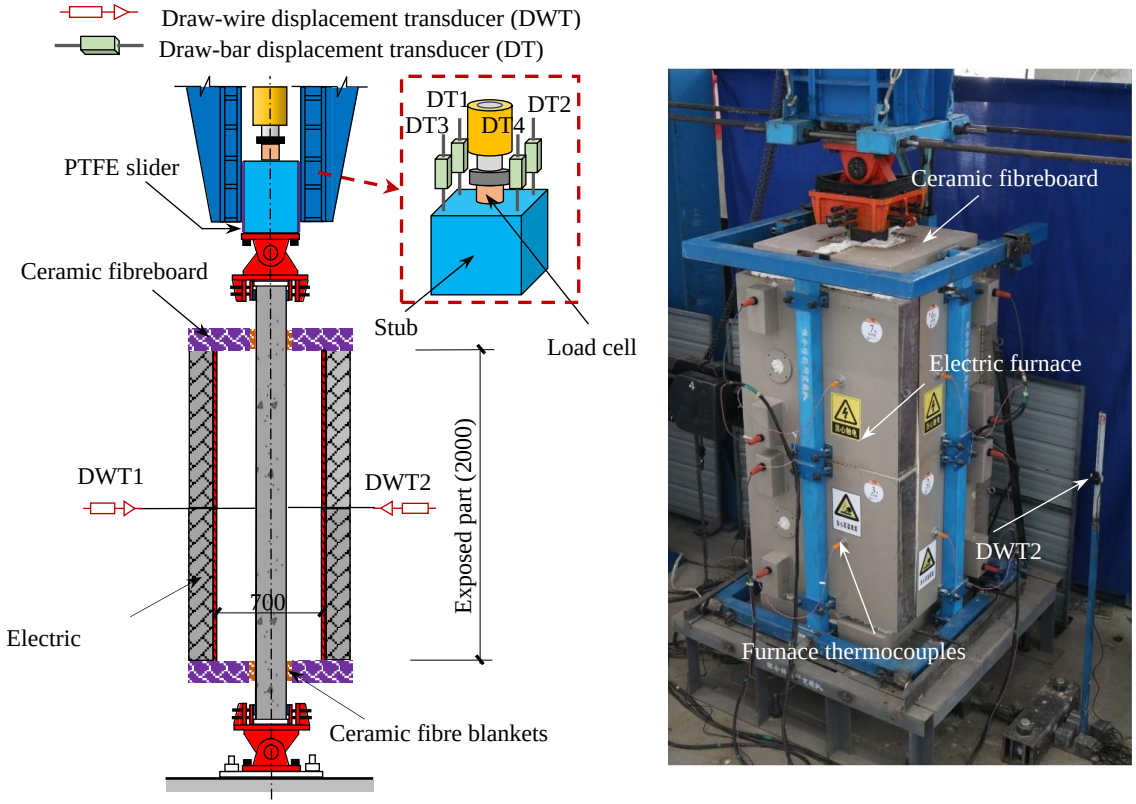

(a) Schematic (b) Photograph of electric furnace

Fig. 5. Setup of fire test (unit: mm)

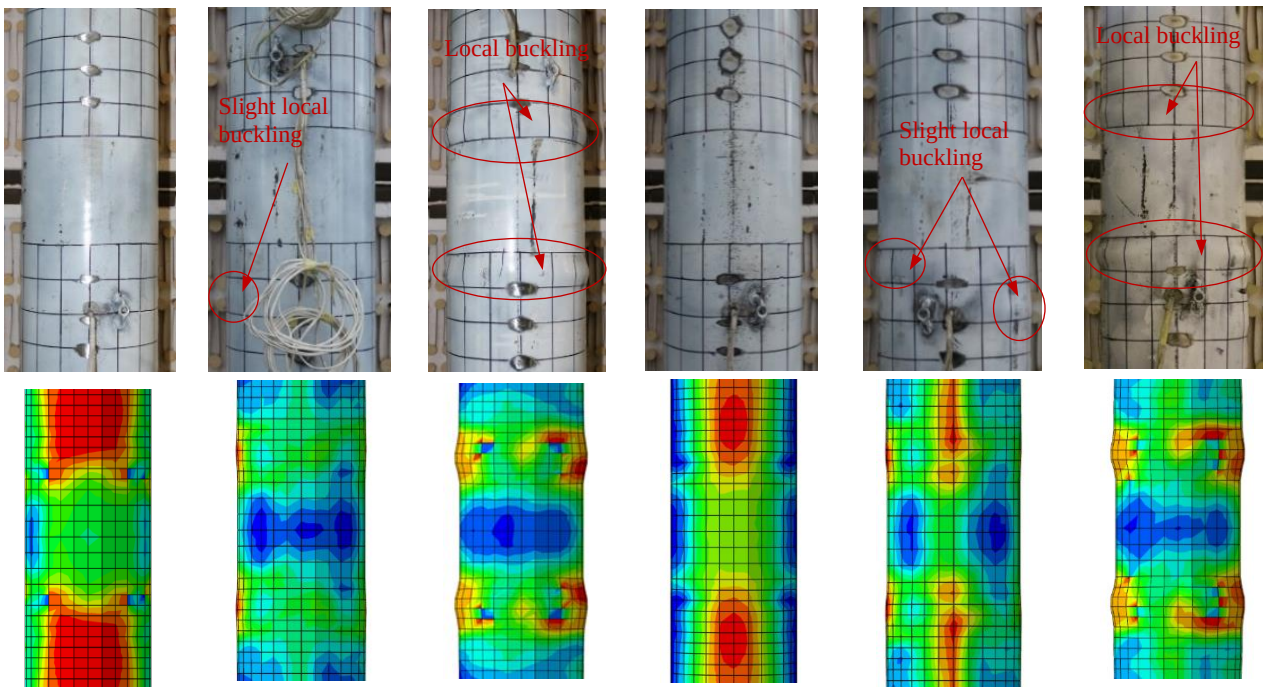

(a) C219-S3 (b) C219-M3 (c) C219-H3 (d) C219-S5 (e) C219-M5 (f) C219-H5

Fig. 6. Column damage after cyclic loading tests

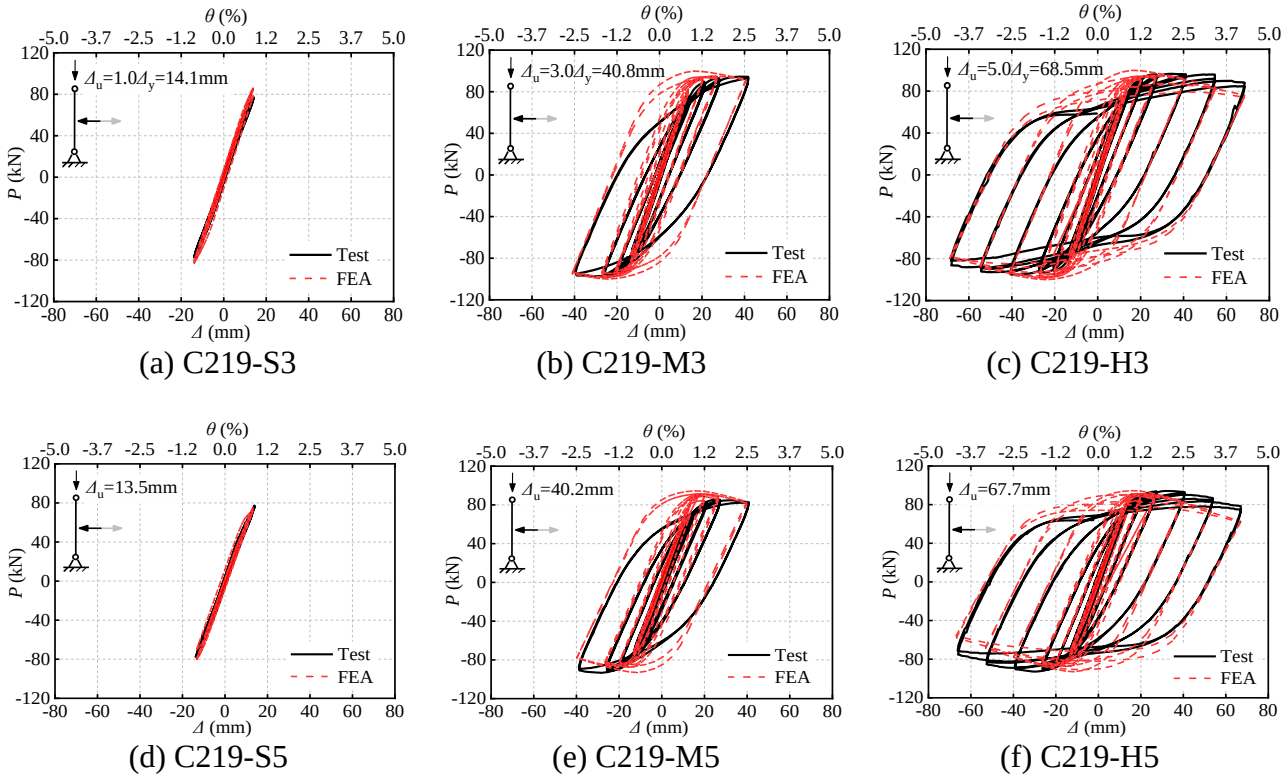

(a) C219-S3 (b) C219-M3 (c) C219-H3

(d) C219-S5 (e) C219-M5 (f) C219-H5

Fig. 7. Lateral load(P)–displacement(Δ) hysteretic curves

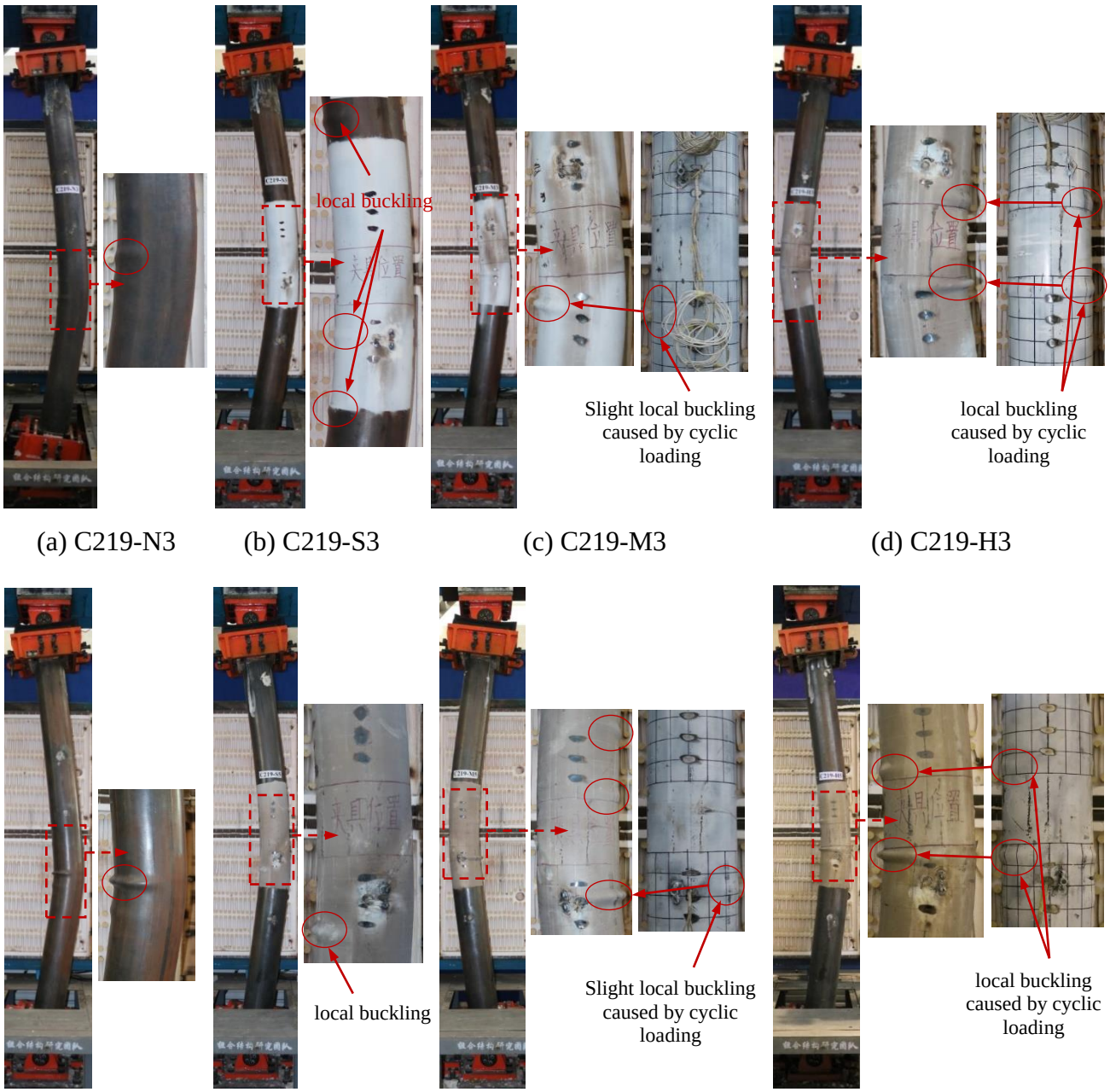

(a) C219-N3 (b) C219-S3 (c) C219-M3 (d) C219-H3

(e) C219-N5 (f) C219-S5 (g) C219-M5 (h) C219-H5

Fig. 8. Failure modes of specimens after fire tests

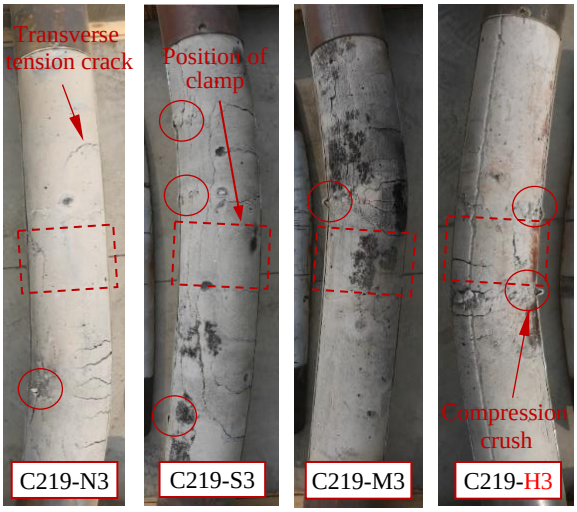

Fig. 9. Failure modes of concrete core

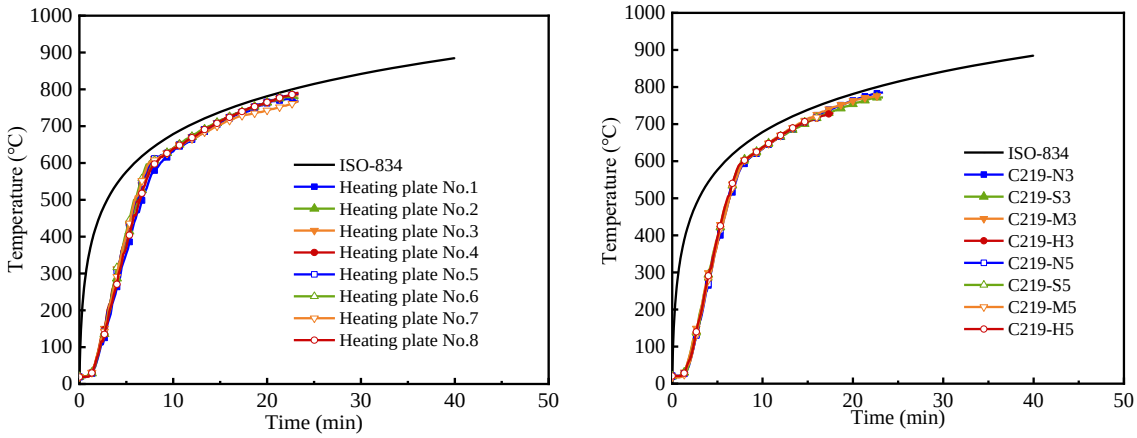

(a) Temperature of heating plate (b) Average furnace temperature

Fig. 10. Furnace temperature

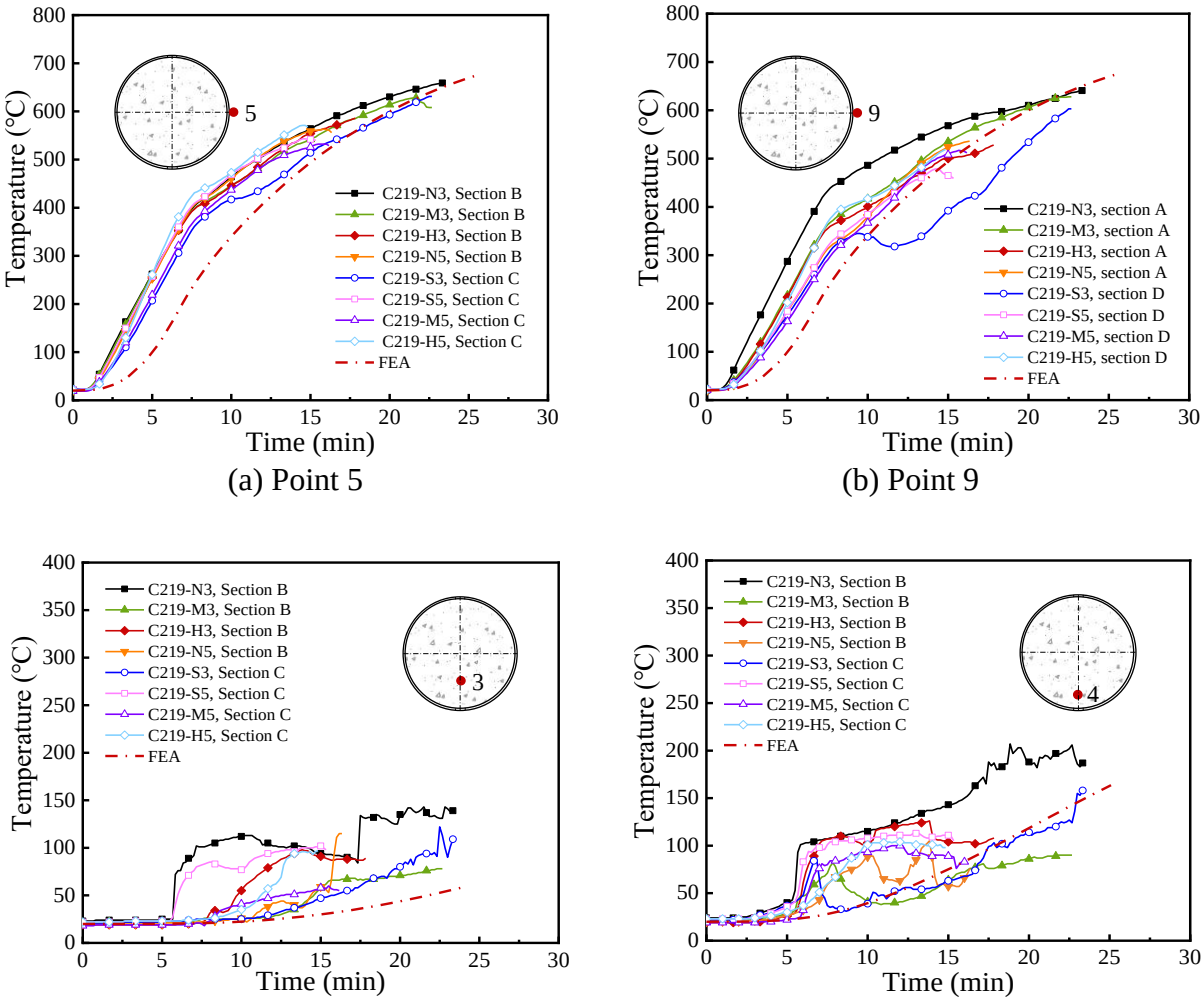

(a) Point 5 (b) Point 9

(c) Point 3 (d) Point 4

Fig. 11. Temperature distribution of specimens

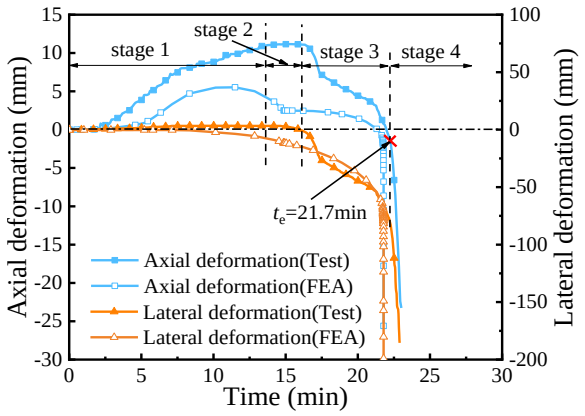

(a) C219-N3

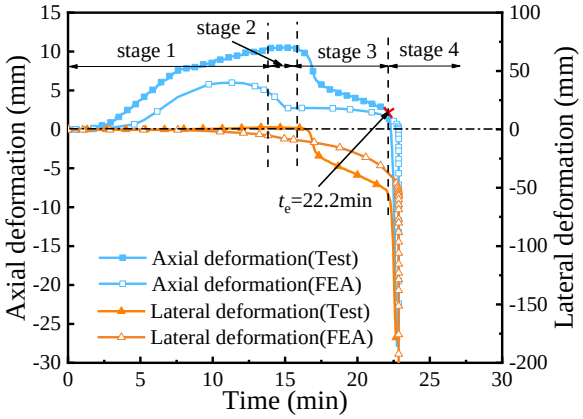

(b) C219-S3

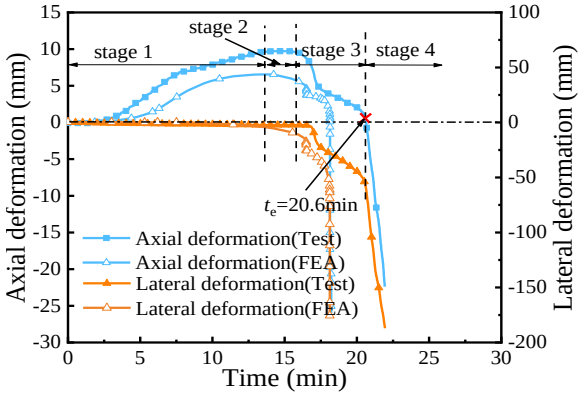

(c) C219-M3

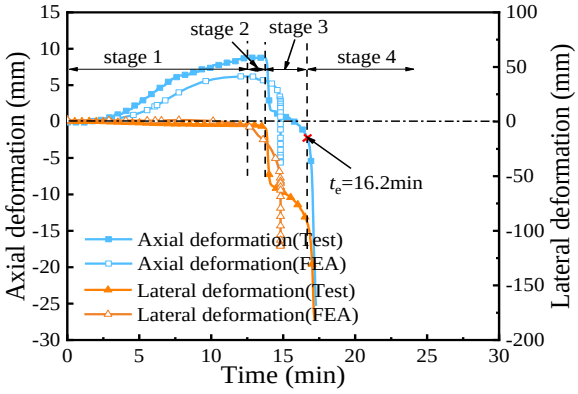

(d) C219-H3

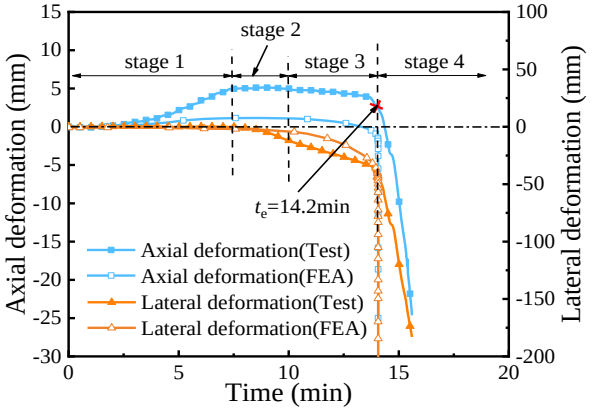

(e) C219-N5

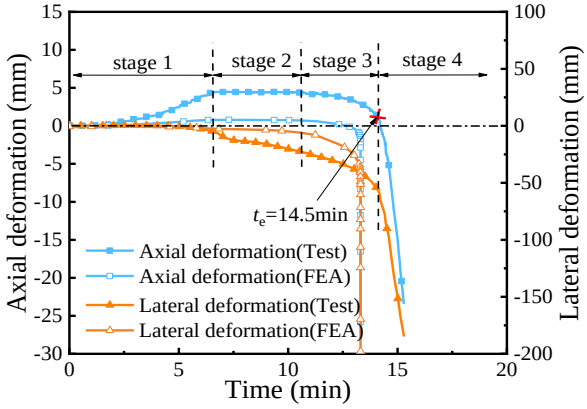

(f) C219-S5

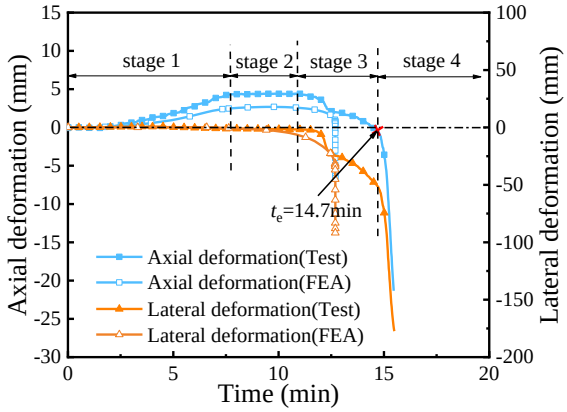

(g) C219-M5

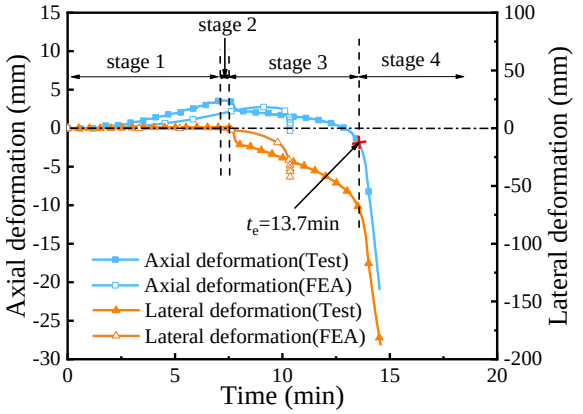

(h) C219-H5

Fig. 12. Deformation-time curves of specimens

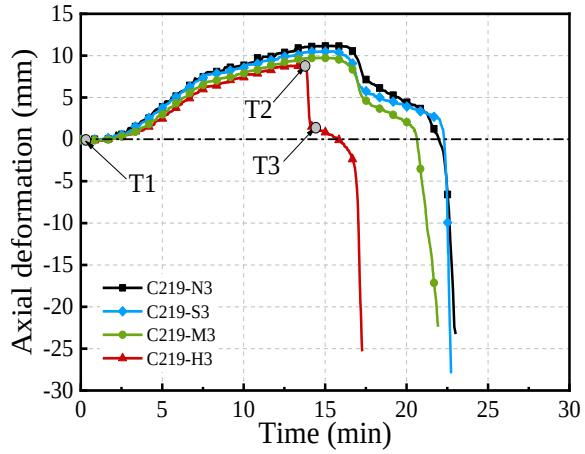

(a) Axial displacement (n=0.284)

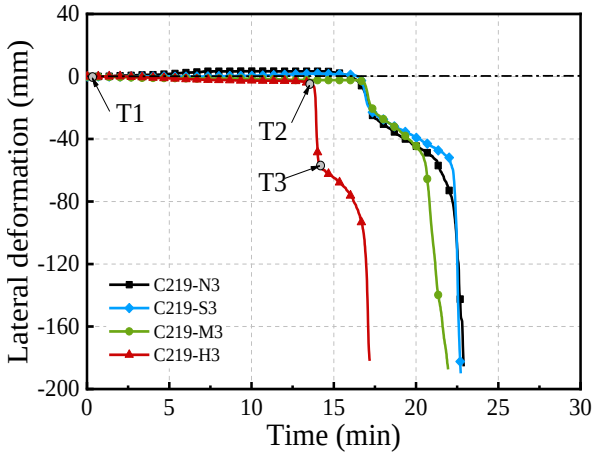

(b) Lateral displacement (n=0.284)

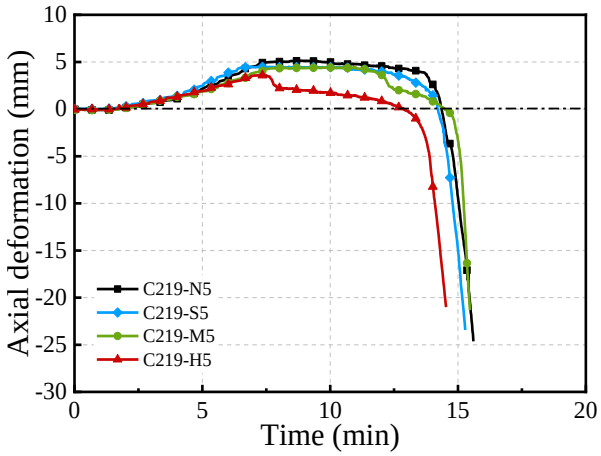

(c) Axial displacement (n=0.431)

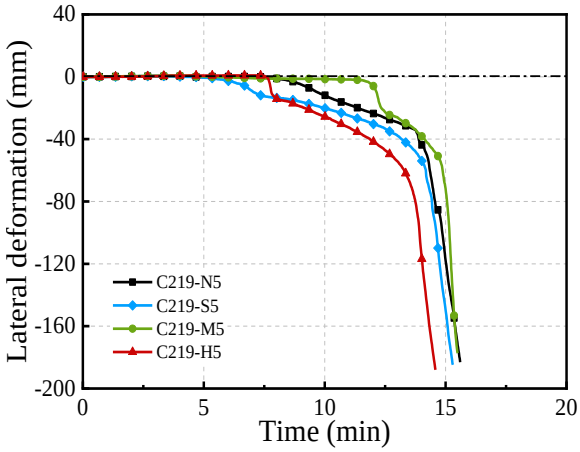

(d) Lateral displacement (n=0.431)

Fig. 13. Comparison of deformation–time curves with different earthquake damage

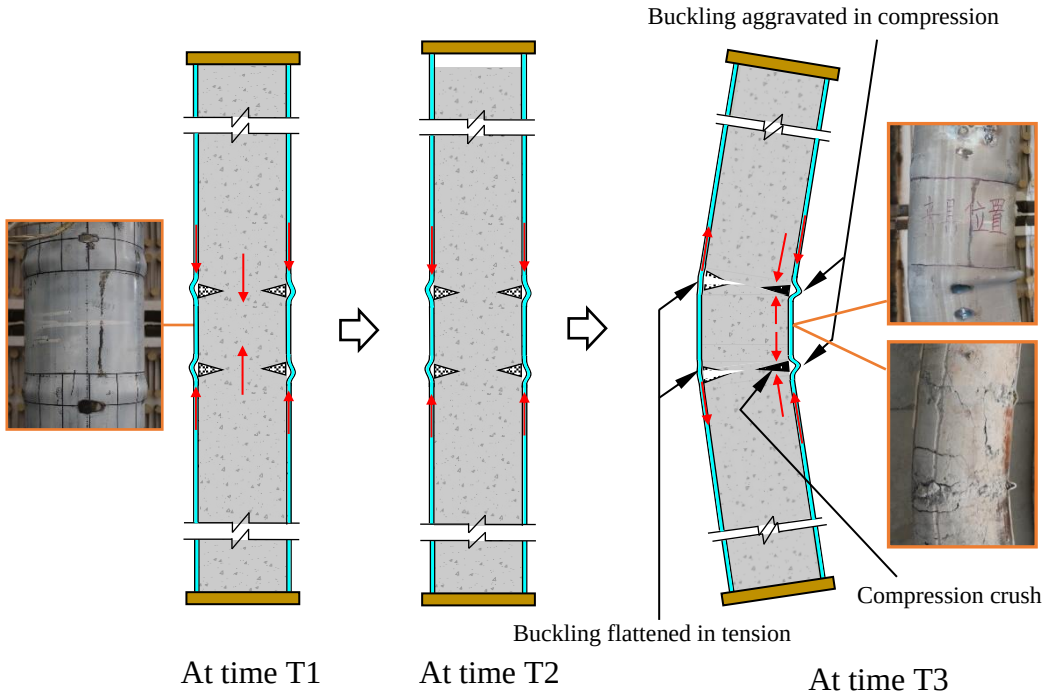

Fig. 14. Influence mechanism of mid-height damage on deformation

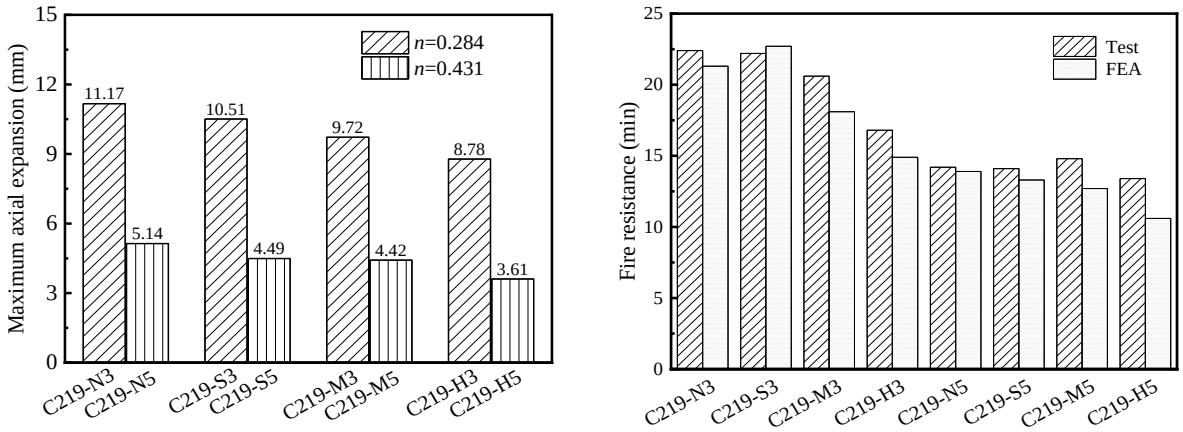

(a) Maximum axial expansion (b) Fire resistance

Fig. 15. Maximum axial expansion deformation and fire resistance

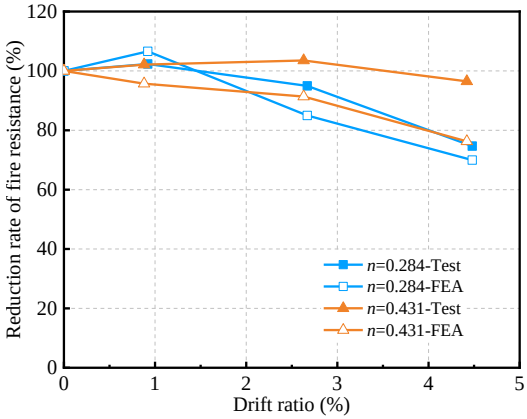

Fig. 16. Effect of axial load ratio and seismic damage level on fire resistance

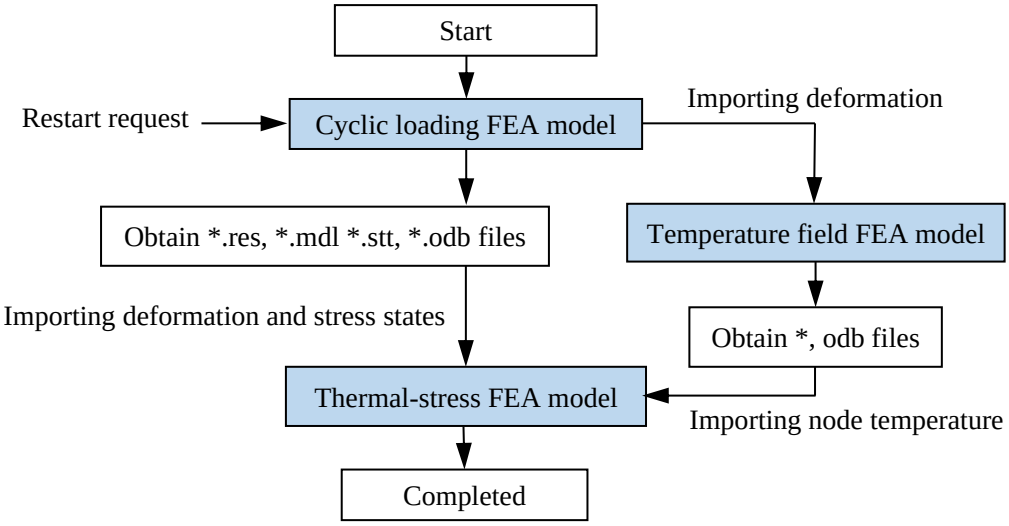

Fig. 17. PEF analysis flowchart

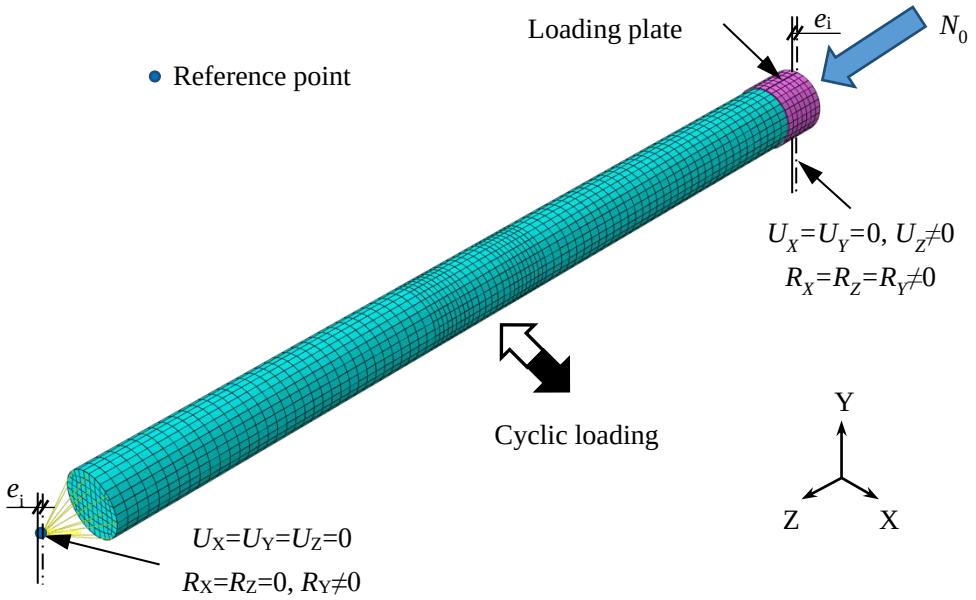

Fig. 18. Meshing and boundary conditions of cyclic loading and thermal-stress FEA model

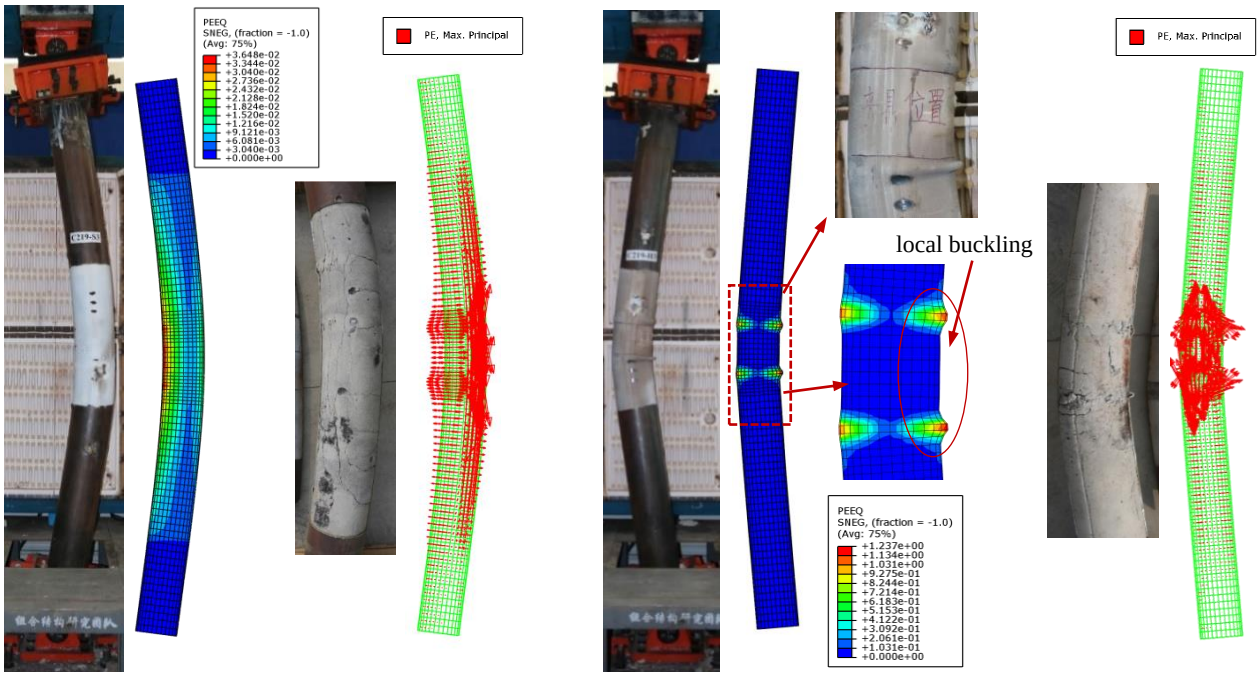

(a) C219-S3 (b) C219-H3

Fig. 19. Comparison of failure modes

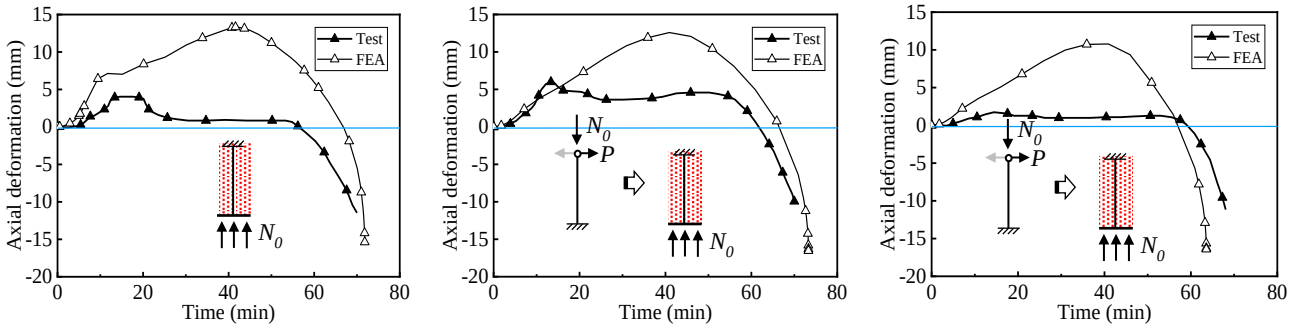

Outer tube: ○203×2.79×2705 mm
Inner tube: ○127×2.29×2705 mm
Damage level: none

(a) S3 (Imani et al., 2015)[34]

Outer tube: ○203×2.79×2705 mm
Inner tube: ○127×2.29×2705 mm
Damage level: moderate

(b) S1 (Imani et al., 2015)[34]

Outer tube: ○203×2.79×2705 mm
Inner tube: ○127×2.29×2705 mm
Damage level: high

(c) S2 (Imani et al., 2015)[34]

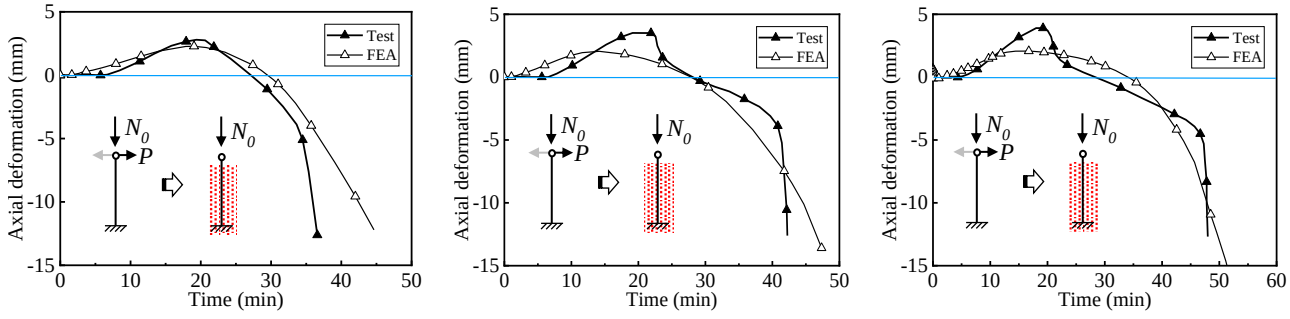

□200×5.7×1080 mm
Damage level: high

(d) T-1 (Wang et al., 2020)[37]

□200×5.7×1080 mm
Damage level: moderate

(e) T-2 (Wang et al., 2020)[37]

□200×5.7×1080 mm
Damage level: slight

(f) T-3 (Wang et al., 2020)[37]

Fig. 20. Comparison of deformation-time curves

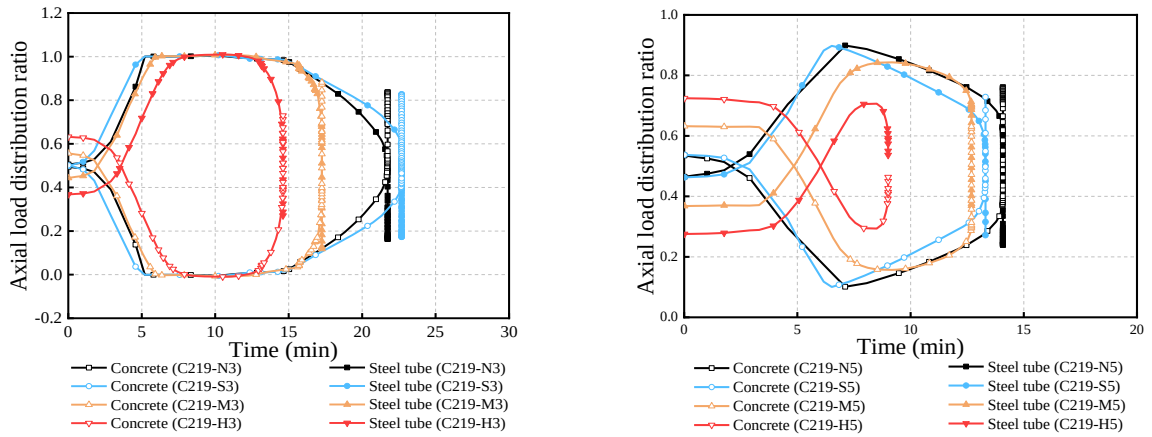

(a) n=0.284 (b) n=0.431

Fig. 21. Axial load distribution of specimens

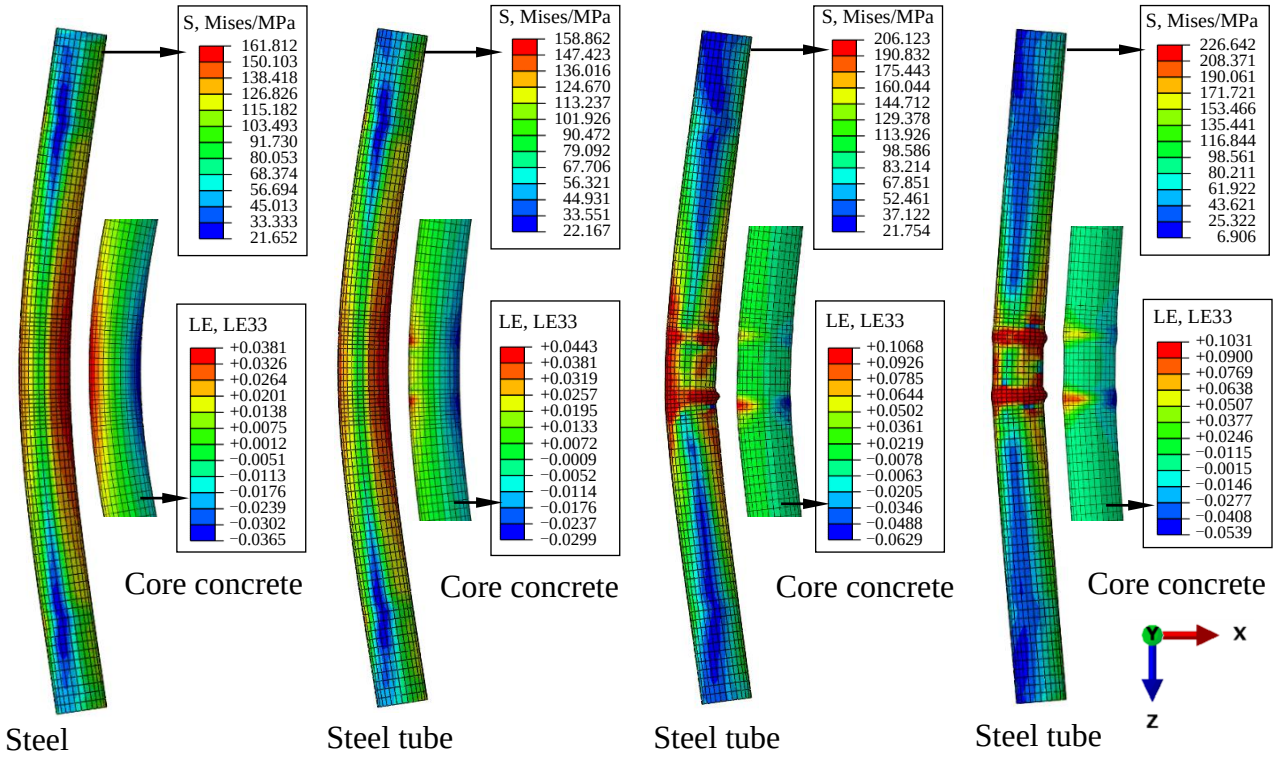

(a) C219-N3 (b) C219-S3 (c) C219-M3 (d) C219-H3

Fig. 22. Comparison of FEA predicted failure modes